NTNU

Norwegian University of
Science and Technology

Modelling Geophysical Properties of Crustal Igneous Rocks

Malin Lerstøl Haaland

Petroleum Geoscience and Engineering
Submission date: June 2017
Supervisor: Kenneth Duffaut, IGP
Co-supervisor: Ketil Hokstad, IGP

Norwegian University of Science and Technology
Department of Geoscience and Petroleum

Abstract

The chemical composition of crustal igneous rocks strongly affects their geophysical properties. In order to model these effects, a classification scheme based on silica content was applied, resulting in the classes felsic, intermediate, mafic and ultramafic. Considering an isotropic linear elastic medium with a particular mineral composition corresponding to a given silica content, upper and lower Hashin-Shtrikman bounds for the elastic moduli and their corresponding compressional and shear wave velocities were estimated as a function of silica content and porosity. These theoretical bounds were compared to rock sample measurements, showing that the bounds represent a good approximation of the individual textural variations. Both elastic moduli, seismic velocities and densities show an increasing trend with decreasing silica content. The self-consistent approximation was applied to model how the elastic properties varies with different pore geometries. Variations in thermal and electrical conductivity as a function of silica content were modelled, which showed quite different trends than for the elastic properties, and in fact seems to be partly opposite correlated.

The Zoeppritz equations were applied in order to model the plane wave reflectivity of theoretical interfaces between an igneous basement overlain by a sedimentary half-space. Results of this shows that the reflectivity generally is stronger for underlying oceanic crust with low silica content (corresponding to the mafic classification) than for continental crust with higher silica content (corresponding to the felsic classification). However, the overlying sedimentary layer plays an important role in controlling the response, as well as other factors. AVA-analysis also indicates why it sometimes can be difficult to identify the basement reflector, especially when interpreting the continental crust. Based on the observations from the reflectivity analysis, the Continental Oceanic Boundary (COB) was attempted interpreted on a seismic line offshore Norway.

Sammendrag

Den kjemiske sammensetningen til magmatiske skorpebergarter påvirker i stor grad deres geofysiske egenskaper. For å modellere denne effekten ble det brukt en klassifikasjonsmodell basert på silika-innhold, som resulterte i kategoriseringen felsisk, intermediær, mafisk og ultramafiske magmatiske bergarter. Ved å anta et isotropisk linært elastisk medium med en bestemt mineralkomposisjon som korresponderer til et gitt silika-innhold ble det estimert øvre og nedre Hashin-Shtrikman grenser for elastisk moduli, samt korresponderende P- og S-bølgehastigheter som funksjon av silika-innhold og porøsitet. Disse teoretiske grensene ble sammenlignet med data fra bergartsprøver, og det ble vist at grensene represerer en god tilnærming av individuelle teksturelle variasjoner. Både elastiske moduli, seismiske hastigheter og tettheter viser en økende trend ved minkende silika-innhold. Den selvkonsistente tilnærmingen ble anvendt for å modellere hvordan de elastiske egenskapene varierer med forskjellige poregeometrier. Variasjoner i termal og elektrisk konduktivitet som funksjon av silika-innhold ble også modellert, og viser svært forskjellige trender enn for elastiske egenskaper, og faktisk synes å være delvis omvendt korrelert.

Zoeppritz-ligningene ble anvendt for å modellere planbølgereflektiviteten til teoretiske grenseflater mellom magmatisk grunnfjell og et overliggende sedimentært halvrom. Resultat av dette viser at reflektiviteten generelt er sterkere for underliggende havskorpe med lavt silika-innhold (korresponderer til mafisk klasse) enn for underliggende kontinentalskorpe med høyere silika-innhold (korresponderer til felsisk klasse), men at det overliggende sedimentlaget spiller en viktig rolle i å kontrollere responsen, samt andre faktorer. AVA-analyse indikerer også hvorfor det kan være vanskelig å identifisere basement-reflektoren, spesielt ved tolkning på kontinental skorpe. Basert på disse observasjonene ble grensen mellom kontinental- og havskorpe (COB) forsøkt tolket på en seismisk linje offshore Norge.

Contents

List of Figures

List of Tables

Nomenclature

α	Aspect ratio for penny-shaped cracks defined by equation 2.31
$\bar{\rho}$	Average density
$\bar{G}^V$	Voigt average for the shear modulus
$\bar{K}^V$	Voigt average for the bulk modulus
$\bar{V_P}$	Average P-wave velocity
$\bar{V_P}^{HS}$	Hashin-Shtrikman average P-wave velocity
$\bar{V_S}$	Average S-wave velocity
$\bar{V_S}^{HS}$	Hashin-Shtrikman average S-wave velocity
β_m	Parameter for the self-consistent approximation defined by equation 2.29
$\Delta\rho$	Density contrast
ΔV_P	P-wave velocity contrast
ΔV_S	S-wave velocity contrast
Γ	Gamma. Defined by equation 2.8
Λ	Lambda. Defined by equation 2.7
λ	Thermal conductivity
λ^{VR+}	Thermal conductivity upper Voigt and Reuss bound

λ^{VR-} Thermal conductivity lower Voigt and Reuss bound

λ_i Thermal conductivity of phase i

λ_{fluid} Thermal conductivity of the fluid

$\lambda_{paralell}$ Thermal conductivity, heat flow paralell to the boundary

λ_{series} Thermal conductivity, heat flow perpendicular to the boundary

ϕ Porosity (fraction)

ρ Density

ρ_i Density of solid phase i

ρ_{bulk} Bulk density

θ_1 Incident angle

θ_2 Reflected/transmitted angle

ζ Zeta. Defined by equation 2.9

ζ_m Parameter for the self-consistent approximation defined by equation 2.30

a Minimum radius of the penny-shaped crack

b Maximum radius of the penny-shaped crack

C Curvature (for the case of the Zoeppritz equations)

c_{33} Thomsen stiffness coefficient

c_{44} Thomsen stiffness coefficient

f_i Volume fraction of phase i

f_i Volume fraction of the inclusion (for the self-consistent approximation)

G Gradient (for the case of the Zoeppritz equations)

G Shear modulus

G^{HS+} Shear modulus upper Hashin-Shtrikman bound

G^{HS-} Shear modulus lower Hashin-Shtrikman bound

G_i Shear modulus of phase i

G_m Bulk modulus of the matrix (for the self-consistent approximation)

G_m The maximum or minimum shear modulus for the two-phased model

G_{fluid} Shear modulus of the fluid

G_i Bulk modulus of the inclusion (for the self-consistent approximation)

G_{max} The maximum shear modulus of the constituent phases

G_{min} The minimum shear modulus of the constituent phases

G^*_{SC} Effective shear modulus

I_P Acoustic impedance for P-wave reflection

I_S Acoustic impedance for S-wave reflection

K Bulk modulus

K^{HS+} Bulk modulus upper Hashin-Shtrikman bound

K^{HS-} Bulk modulus lower Hashin-Shtrikman bound

K_i Bulk modulus of phase i

K_m Bulk modulus of the matrix (for the self-consistent approximation)

K_m The maximum or minimum bulk modulus for the two-phased Hashin-Shtrikman-Walpole model

K_{fluid} Bulk modulus of the fluid

K_i Bulk modulus of the inclusion (for the self-consistent approximation)

K_{max} The maximum bulk modulus of the constituent phases

K_{min} The minimum bulk modulus of the constituent phases

K^*_{SC} Effective bulk modulus

M Matrix used in the Zoeppritz equation defined by equation 2.40

N Matrix used in the Zoeppritz equation defined by equation 2.41

P Geometrical factor for the self-consistent approximation defined in table 2.1

p Ray parameter

$P^{*fluid,1}$ Geometrical factor of spherical inclusions filled with a fluid

$P^{*fluid,2}$ Geometrical factor of penny-shaped inclusions filled with a fluid

Q Geometrical factor for the self-consistent approximation defined in table 2.1

$Q^{*fluid,1}$ Geometrical factor of spherical inclusions filled with a fluid

$Q^{*fluid,2}$ Geometrical factor of penny-shaped inclusions filled with a fluid

R_0 Reflection coefficient for zero incidence

R_{PP} Reflection coefficient for P-P reflection

R_{PS} Reflection coefficient for P-S reflection

R_{SP} Reflection coefficient for S-P reflection

R_{SS} Reflection coefficient for S-S reflection

V_P P-wave velocity

V_P^{HS+} P-wave velocity upper Hashin-Shtrikman bound

V_P^{HS-} P-wave velocity lower Hashin-Shtrikman bound

V_S S-wave velocity

V_S^{HS+} S-wave velocity upper Hashin-Shtrikman bound

V_S^{HS-} S-wave velocity lower Hashin-Shtrikman bound

Chapter 1

Introduction

1.1 Background

Igneous rocks are the most abundant rocks in the crust, commonly divided into the continental crust and the oceanic crust. The Continental-Oceanic Boundary (COB) represents the transition between the oceanic and the continental crust. The oceanic crust is mainly made up of basalt (Christensen et al., 1980), and is generally darker and denser than the oceanic crust, because of a high content of high-density ferromagnesian minerals. The oceanic crust is also significantly thinner than the continental crust; usually about 6 to 7 km thick (Barton, 2006), while Christensen and Mooney (1995) estimates the weighted average thickness of the continental crust to be 41.1 km. Silica-rich rock types, especially granites, dominates the continental crust. Because of their differences in appearance, their geophysical properties also differ, and it is important to understand which factors controls these differences.

The study of sedimentary rocks has mainly been the focus in petroleum exploration because they form the main components of a petroleum system. But the sedimentary rocks only represents a part of the uppermost crust, overlying an igneous basement. In order to obtain a broader understanding of the complex forming of a hydrocarbon system in the crust, the study of igneous rocks is essential.

Identifying the geophysical properties of the crust is important in order to determine other properties that are of direct interest for application in hydrocarbon exploration. Common geophysical properties of interest includes both mechanical properties such as elasticity and

density, electromagnetic and thermal properties such as resistivity, thermal conductivity and magnetic susceptibility. Various geophysical methods are commonly used to measure or estimate these properties directly or indirectly, and the properties can be related through several correlations controlled by physical parameters.

1.2 Problem and delimination

For classification of igneous rocks, a simple known model is used based on the chemical composition of the rock, described by Schön (2015a). This chemical model suggests that acid rocks have a silica content (chemical content of SiO_2) of more than 63 wt%, intermediate rocks between 52-63 wt% silica, basic rocks between 45-52 wt% silica and ultrabasic have a silica content of less than 45 wt%. Because the mineralogical composition of rocks is determined by their chemical content, the classification model based on mineral content, it is further assumed that the acid term corresponds to the felsic term, basic to mafic and ultrabasic to ultramafic, even though this terminology is based on mineralogical classification and not chemical directly. The mineral composition, and hence the silica content plays a large role in controlling the physical properties of rocks. It is known that both seismic velocity, density, specific gravity and darkness generally increases with decreasing silica content, due to the corresponding change in mineral composition.

Because the model considers the chemical composition of a rock, chemical analysis of the rock is required. Chemical analysis can be performed by XRD (X-Ray Diffraction) analysis in the lab, but cannot be performed by studying hand specimens in the field. The model does not separate between volcanic (extrusive) and plutonic (intrusive) rocks in the classification. It is known that textural factors have a significant impact on the geophysical properties of rocks, and the uncertainty related to the possible textural variations are therefore accounted for by implementing upper and lower bounds. The effect of varying pore geometries can be further modelled by approximations, for example the self-consistent approximation.

There are other classification models based on the texture of the rock, as well as other more complicated models based on chemical content and mineral content. But because the purpose of this thesis is to obtain a view of the geophysical properties of igneous rocks considering the

differences between continental and the oceanic crust, the chemical model that incorporates the composition of the rock is the most relevant for this case. Classification of igneous rocks based on this model is essential in order to detect how their geophysical properties change with their chemical composition.

The main objective of this thesis is to investigate the geophysical properties of igneous rocks given their composition, in order to model how their geophysical properties changes with change in silica content. This is done by specific assumptions of elastic, thermal and electric properties and densities of the constituent phases, as well as their volume fractions as a function of silica content. These parameters were incorporated into theoretical upper and lower bounds for a composite containing a mixture of constituents given by the classification model.

We know that geophysical properties, especially mechanical properties depends greatly on porosity, and therefore it is necessary to account for the porosity of the rock when performing the estimations. The fluid to fill the pore space was assumed to be brine or pure water (H_2O). Temperature and pressure conditions also affects the geophysical properties of rocks, and hence it is important that the effect of changes in these parameters are considered. For the sake of simplicity, standard temperature ($20°C$) and pressure conditions (1 atm $\approx$ 0.1 MPa) are considered both for the model and when comparing the model with data. Christensen and Mooney (1995) shows that the anisotropy is quite small for igneous rocks (usually less than 2% at 1 GPa), so the effect of anisotropy is neglected, and an elastic isotropic composite is assumed.

1.3 Structure of the thesis

- Chapter 2 presents the theoretical background that forms the basis for the calculations and estimations presented in this thesis. The theory includes calculation of the Hashin-Shtrikman bounds for elastic properties, Voigt and Reuss bounds for thermal conductivity, the self-consistent approximation for modelling of pore geometries and the Zoeppritz equations for reflectivity modelling.

- Chapter 3 describes the methods applied for obtaining the results, as well as the as-

sumptions made. Properties used for calculations are also presented. The chemical classification model is described as the primary basis for estimation of theoretical bounds and further modeling of elastic, thermal and electrical properties.

- Chapter 4 presents the main results obtained in terms of figures and descriptions. The results include theoretical models estimated based on the classification model, as well as real data in terms of core measurements, pressure data and seismic.
- Chapter 5 presents a thorough discussion about the results, comparison between the theoretical models and real data, the uncertainties and limitations of the methods used, and suggestions for improvements.
- Chapter 6 presents the main conclusions from this thesis in terms of bullet points.
- Chapter 7 presents proposals for further work.

Chapter 2

Theory

2.1 Hashnin-Shtrikman bounds

The theoretical background for the approach of predicting the elastic moduli for an elastic composite without specifying the geometries of the constituent phases, is by incorporating Hashin-Shtrikman bounds.

The Hashin-Shtrikman bounds are defined as the best bounds for an isotropic linear elastic composite giving the narrowest possible range without specifying anything about the geometries of the constituents (Hashin and Shtrikman, 1963). They are extremely robust and relatively free of idealizations and approximations (Avseth et al., 2010). In order to predict the specific effective elastic moduli of a mixture of phases (grains and pores), the volume fractions and the elastic properties of the seperate phases has to be be specified, as well as their geometries. If the geometries of how the phases are related relative to each other are not specified, the most accurate prediction of the elastic moduli of the composite is obtained by specifying the upper and lower bounds. Typically, rocks containing stiff pore shapes will be oriented close to the upper bound, while rocks containing soft pore shapes will be close to the lower bound (Mavko et al., 2009).

For a two-phase model, the bounds for the bulk and shear moduli, here denoted K and G respectively, is described by equation 2.1 and 2.2 respectively. f_1 and f_2 are the the volume fractions of phase 1 and 2 respectively, K_1 and K_2 their bulk moduli, and G_1 and G_2 their shear moduli. The equations yield the upper bound when the stiffest material

(largest moduli) is termed 1 and K_m and G_m are the maximum bulk and shear moduli of the constituents, and the lower bound when the softest material is termed 1 and. and K_m and G_m are the minimum bulk and shear moduli. These bounds are sometimes called the Hashin-Shtrikman Walpole bounds, because they account for the fact that the constituent with largest bulk moduli may don't have the largest shear moduli, even though this is usually the case.

$$K^{HS\pm} = K_1 + \frac{f_2}{(K_2 - K_1)^{-1} + f_1(K_1 + \frac{4}{3}G_m)^{-1}} \tag{2.1}$$

$$G^{HS\pm} = G_1 + \frac{f_2}{(G_2 - G_1)^{-1} + f_1[G_1 + \frac{G_m}{6}(\frac{9K_m+8G_m}{K_m+2G_m})]^{-1}} \tag{2.2}$$

Berryman (1995) introduces a general form of the bounds which can be applied for a mixture of more than two phases. The upper and lower bounds for the bulk modulus for a mixture of several phases are given by equations 2.3 and 2.4 respectively. The bulk modulus of such a composite consisting of a mixture of constituents therefore has to plot in between these upper and lower bounds for a given silica content. G_{max} and G_{min} corresponds to the maximum and the minimum shear modulus of the constituents, and includes both solid and fluid phases.

$$K^{HS+} = \Lambda(G_{max}) \tag{2.3}$$

$$K^{HS-} = \Lambda(G_{min}) \tag{2.4}$$

Equations 2.5 and 2.6 define the upper and lower bounds for the shear modulus. The same principle as for the bounds for the bulk modulus also applies for these bounds. K_{max} and K_{min} corresponds to the maximum and the minimum bulk modulus of the constituents. For a fluid, we know that the shear modulus is equal to zero, meaning that G_{min} also will be equal to zero for all other porosities than zero if the pore space is filled with a fluid.

$$G^{HS+} = \Gamma(\zeta(K_{max}, G_{max})) \tag{2.5}$$

$$G^{HS-} = \Gamma(\zeta(K_{min}, G_{min})) \tag{2.6}$$

Λ, Γ and ζ are defined by equations 2.7, 2.8 and 2.9 respectively.

$$\Lambda(z) = \left\langle \frac{1}{K(r) + \frac{4}{3}z} \right\rangle^{-1} - \frac{4}{3}z \tag{2.7}$$

$$\Gamma(z) = \left\langle \frac{1}{G(r) + z} \right\rangle^{-1} - z \tag{2.8}$$

$$\zeta(K, G) = \frac{G}{6}\left(\frac{9K + 8G}{K + 2G}\right) \tag{2.9}$$

For a mixture of n solid phases with fractions f_1, ... , f_n of the solid matrix, a single fluid phase and a given porosity ϕ, the bounds for the bulk modulus are then defined by equation 2.10, where K_1, ... , K_n are the corresponding bulk modulus of the given phase. G=G_{max} yields the upper bound, and G=G_{min} yields the lower bound.

$$K^{HS\pm} = \left(\frac{\phi}{K_{fluid} + \frac{4}{3}G} + \sum_{i=1}^{n}\left\{\frac{(1-\phi)f_i}{K_i + \frac{4}{3}G} + ... + \frac{(1-\phi)f_n}{K_n + \frac{4}{3}G}\right\}\right)^{-1} - \frac{4}{3}G \tag{2.10}$$

The bounds for the shear modulus are further defined by equation 2.11. G_1, ... , G_n are the corresponding shear modulus of the phases. $\zeta(K_{max}, G_{max})$ yields the upper bound and $\zeta(K_{min}, G_{min})$ the lower bound.

$$G^{HS\pm} = \left(\frac{\phi}{G_{fluid} + \zeta(K, G)} + \sum_{i=1}^{n}\left\{\frac{(1-\phi)f_i}{G_i + \zeta(K, G)} + ... + \frac{(1-\phi)f_n}{G_n + \zeta(K, G)}\right\}\right)^{-1} - \zeta(K, G) \tag{2.11}$$

2.2 Compressional and shear wave velocity

The velocities of seismic waves depends on the elastic moduli of the constituents of the medium that the waves are travelling through. They can be expressed in terms of the bulk modulus, the shear modulus and the bulk density (denoted ρ_{bulk}). The bulk density of a composite consisting of a fluid phase with density ρ_{fluid}, solid phases with fractions f_i and densities ρ_i and porosity ϕ is given by equation 2.14.

The compressional wave is referred to as the primary wave or the P-wave. For an isotropic medium, its velocity is described by equation 2.12. The shear wave is referred to as the secondary or S-wave. Its velocity is described by equation 2.13.

$$V_P = \sqrt{\frac{K + \frac{4}{3}G}{\rho_{bulk}}} \tag{2.12}$$

$$V_S = \sqrt{\frac{G}{\rho_{bulk}}} \tag{2.13}$$

$$\rho_{bulk} = \phi\rho_{fluid} + \sum_{i=1}^{n}(1-\phi)f_i\rho_i + ... + (1-\phi)f_n\rho_n \tag{2.14}$$

Bounds for the compressional and shear wave velocities are obtained by incorporating the Hashin-Shtrikman bounds for the elastic moduli; the bulk modulus and the shear modulus. Compressional and shear wave velocity bounds are obtained by applying equations 2.15 and 2.16 respectively. K^{HS+} and G^{HS+} yields the upper velocity bounds (V_P^{HS+} and V_S^{HS+}), and K^{HS-} and G^{HS-} yields the lower velocity bounds (V_P^{HS-} and V_S^{HS-}).

$$V_P^{HS\pm} = \sqrt{\frac{K^{HS\pm} + \frac{4}{3}G^{HS\pm}}{\rho_{bulk}}} \tag{2.15}$$

$$V_S^{HS\pm} = \sqrt{\frac{G^{HS\pm}}{\rho_{bulk}}} \tag{2.16}$$

An Hashin-Shrikman average can be useful in order to give an estimate of a property based on the upper and lower bounds. The Hashin-Shtrikman average of the compressional and shear wave velocity bounds ($\bar{V_P}^{HS}$ and $\bar{V_S}^{HS}$) is given by equation 2.17 and 2.18 respectively.

$$\bar{V_P}^{HS} = \frac{V_P^{HS+} + V_P^{HS-}}{2} \tag{2.17}$$

$$\bar{V_S}^{HS} = \frac{V_S^{HS+} + V_S^{HS-}}{2} \tag{2.18}$$

For a transversely isotropic medium with weak anisotropy, the compressional and shear wave velocities can be expressed by the stiffness coefficients (Thomsen, 1986) as defined by equations 2.19 and 2.20 for P-wave velocity and S-wave velocity respectively.

$$V_P = \sqrt{\frac{c_{33}}{\rho}} \tag{2.19}$$

$$V_S = \sqrt{\frac{c_{44}}{\rho}} \tag{2.20}$$

2.3 Voigt and Reuss bounds

An approach of predicting the thermal conductivity (denoted λ) of a composite was introduced by Voigt and Reuss (Schön, 2015b) by considering a layered model. This concept is also discussed by Mavko et al. (2009). The theoretical upper bound is defined by the parallel model (equation 2.21), where the heat flow is considered to be parallel to the boundary between the constituents. In contrast, the theoretical lower bound is defined by the series model (equation 2.22), where the heat flow is considered to be perpendicular to the boundary.

$$\lambda_{parallel} = \sum_{i=1}^{n} f_i \lambda_i \tag{2.21}$$

$$\lambda_{series} = \left[\sum_{i=1}^{n} f_i \lambda_i^{-1} \right]^{-1} \tag{2.22}$$

Hence, for a mixture of n solid phases with fractions f_1, ... , f_n of the solid matrix, a single fluid phase and a given porosity ϕ, the Voigt and Reuss upper and lower bounds for the thermal conductivity are further defined by equations 2.23 and 2.24. λ^{VR+} yields the

upper bound and λ^{VR-} the lower bound.

$$\lambda^{VR+} = \phi\lambda_{fluid} + \sum_{i=1}^{n}(1-\phi)f_i\lambda_i \tag{2.23}$$

$$\lambda^{VR-} = \left[\phi\lambda_{fluid}^{-1} + \sum_{i=1}^{n}(1-\phi)f_i\lambda_i^{-1}\right]^{-1} \tag{2.24}$$

The Voigt average for the bulk and shear modulus ($\bar{K}^V$ and $\bar{G}^V$) is given by equations 2.25 and 2.26 respectively (Mavko et al., 2009).

$$\bar{K}^V = \sum_{i=1}^{n} f_i K_i \tag{2.25}$$

$$\bar{G}^V = \sum_{i=1}^{n} f_i G_i \tag{2.26}$$

2.4 The self-consistent approximation of effective moduli

Assuming specific inclusion shapes, one can predict the elastic moduli of a composite, given the volume fraction of the constituents as well as their elastic properties. The self-consistent approximation considers the elastic deformation of isolated inclusions, where the interaction of inclusions is approximated by an unknown effective medium (Mavko et al., 2009).

Te Wu (1966) describes an estimate of the elastic moduli by the self-consistent approximation for two-phase composites. This estimate is described by equation 2.27 and 2.28 for the bulk modulus and shear modulus respectively.

$$K_{SC}^* = K_m + f_i(K_i - K_m)P^{*i} \tag{2.27}$$

$$G_{SC}^* = G_m + f_i(G_i - G_m)Q^{*i} \tag{2.28}$$

Here, K_{Sc}^* and G_{Sc}^* represents the effective bulk modulus and shear modulus respectively.

Table 2.1: Geometrical factors P and Q for spherical and penny shaped inclusions

Inclusion shape	P^{mi}	Q^{mi}
Spheres	$\frac{K_m+\frac{4}{3}G_m}{K_i+\frac{4}{3}G_m}$	$\frac{G_m+\zeta_m}{G_i+\zeta_m}$
Penny cracks	$\frac{K_m+\frac{4}{3}G_i}{K_i+\frac{4}{3}G_i+\pi\alpha\beta_m}$	$\frac{1}{5}\left[1+\frac{8G_m}{4G_i+\pi\alpha(G_m+2\beta_m}+2\frac{K_i+\frac{2}{3}(G_i+G_m)}{K_i+\frac{4}{3}G_i+\pi\alpha\beta_m}\right]$

Figure 2.1: Illustation of the aspect ratio α for penny shaped inclusions

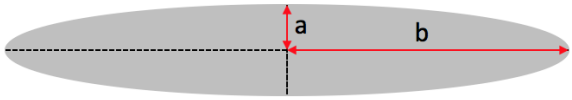

K_m and G_m are the moduli of the matrix, while K_i and G_i are the moduli of the inclusion. f_i is the volume fraction of the inclusion, while P and Q are geometrical factors, given by the geometry of the inclusion. The geometrical factors are given by table 2.1. The parameters β_m and ζ_m are given by equation 2.29 and 2.30 respectively. α is the aspect ratio of the penny shaped cracks illustrated in figure 2.1 and defined by equation 2.31.

$$\beta_m = G_m \frac{3K_m + G_m}{3K_m + 4G_m} \tag{2.29}$$

$$\zeta_m = \left(\frac{G_m}{6}\right) \frac{9K_m + 8G_m}{K_m + 2G_m} \tag{2.30}$$

$$\alpha = \frac{a}{b} \quad (0 \leq \alpha \leq 1) \tag{2.31}$$

A general approach for predicting the elastic moduli of an effective medium for n phase constituents is described by Berryman (1995) through equations 2.32 and 2.33 for the bulk and shear modulus respectively.

$$\sum_{i=1}^{n} f_i(K_i - K^*_{SC})P^{*i} = 0 \tag{2.32}$$

$$\sum_{i=1}^{n} f_i(G_i - G^*_{SC})Q^{*i} = 0 \tag{2.33}$$

For a composite with a porosity ϕ and a combination of spherical and penny shaped in-

clusions, the effective moduli K^*_{SC} and G^*_{SC} can be modelled by solving the coupled equations 2.34 and 2.35. Here, f_1 represents the porosity fraction of spherical cracks, and f_2 represents the porosity fraction of penny shaped cracks. $P^{*fluid,1}$ and $Q^{*fluid,1}$ represents the geometrical factors of spherical inclusions filled with a certain fluid with bulk modulus K_{fluid} and shear modulus G_{fluid}. $P^{*fluid,2}$ and $Q^{*fluid,2}$ corresponds to the geometrical factors of penny shaped inclusions with the same fluid properties.

$$\sum_{i=1}^{n}(1-\phi)(K_{solid}-K^*_{SC})+\phi f_1(K_{fluid}-K^*_{SC})P^{*fluid,1}+\phi f_2(K_{fluid}-K^*_{SC})P^{*fluid,2}=0 \quad (2.34)$$

$$\sum_{i=1}^{n}(1-\phi)(G_{solid}-G^*_{SC})+\phi f_1(G_{fluid}-G^*_{SC})Q^{*fluid,1}+\phi f_2(G_{fluid}-G^*_{SC})Q^{*fluid,2}=0 \quad (2.35)$$

2.5 AVO/AVA analysis and Zoeppritz equations

AVO (amplitude versus offset) or AVA (amplitude versus angle) analysis is the study of how amplitudes vary with offset or incident angle at a planar horizontal interface. The normal incidence reflection coefficient is defined as the ratio of the reflected wave amplitude to the incident wave amplitude for an incident angle equal to zero. For the interface between an overlying half-space (denoted layer 1) and an underlying half-space (denoted layer 2) the reflection coefficient is defined by equations 2.36 and 2.36 for P-P wave reflection and S-S wave reflection respectively. The acoustic impedance is denoted I, defined as the product of density and velocity.

$$R_{PP} = \frac{\rho_2 V_{P2} - \rho_1 V_{P1}}{\rho_2 V_{P2} + \rho_1 V_{P1}} = \frac{I_{P2} - I_{P1}}{I_{P2} + I_{P1}} \quad (2.36)$$

$$R_{SS} = \frac{\rho_2 V_{S2} - \rho_1 V_{S1}}{\rho_2 V_{S2} + \rho_1 V_{S1}} = \frac{I_{S2} - I_{S1}}{I_{S2} + I_{S1}} \quad (2.37)$$

For non-normal incidence the reflection and transmission coefficients depends on the angle of incidence, or the offset. Snell's law describes the relation of the incident, reflected and

transmitted angles, defined by equation 2.39 where p is the ray parameter.

$$p = \frac{sin\theta_1}{V_{P1}} = \frac{sin\theta_2}{V_{P2}} = \frac{sin\theta_1}{V_{S1}} = \frac{sin\theta_2}{V_{S2}} \tag{2.38}$$

The Zoeppritz equations gives the complete solution for the amplitudes of transmitted and reflected P- and S-waves for non-normal incidence (Aki and Richards, 1980). Equation 2.39 shows this solution, where the matrices M and N are defined by equations 2.40 and 2.41 respectively.

$$\begin{bmatrix} \grave{P}\acute{P} & \grave{S}\acute{P} & \acute{P}\acute{P} & \acute{S}\acute{P} \\ \grave{P}\acute{S} & \grave{S}\acute{S} & \acute{P}\acute{S} & \acute{S}\acute{S} \\ \grave{P}\grave{P} & \grave{S}\grave{P} & \acute{P}\grave{P} & \acute{S}\grave{P} \\ \grave{P}\grave{S} & \grave{S}\grave{S} & \acute{P}\grave{S} & \acute{S}\grave{S} \end{bmatrix} = M^{-1}N \tag{2.39}$$

$$M = \begin{pmatrix} -sin\theta_1 & -cos\theta_{S1} & sin\theta_2 & cos\theta_{S2} \\ cos\theta_1 & -sin\theta_{S1} & cos\theta_2 & -sin\theta_{S2} \\ 2\rho_1 V_{S1} sin\theta_{S1} cos\theta_1 & \rho_1 V_{S1}(1-2sin^2\theta_{S1}) & 2\rho_2 V_{S2} sin\theta_{S2} cos\theta_2 & \rho_2 V_{S2}(1-2sin^2\theta_{S2}) \\ -\rho_1 V_{P1}(1-2sin^2\theta_{S1}) & \rho_1 V_{S1} sin2\theta_{S1} & \rho_2 V_{P2}(1-2sin^2\theta_{S2}) & -\rho_2 V_{S2} sin2\theta_{S2} \end{pmatrix} \tag{2.40}$$

$$N = \begin{pmatrix} sin\theta_1 & cos\theta_{S1} & -sin\theta_2 & -cos\theta_{S2} \\ cos\theta_1 & -sin\theta_{S1} & cos\theta_2 & -sin\theta_{S2} \\ 2\rho_1 V_{S1} sin\theta_{S1} cos\theta_1 & \rho_1 V_{S1}(1-2sin^2\theta_{S1}) & 2\rho_2 V_{S2} sin\theta_{S2} cos\theta_2 & \rho_2 V_{S2}(1-2sin^2\theta_{S2}) \\ \rho_1 V_{P1}(1-2sin^2\theta_{S1}) & -\rho_1 V_{S1} sin2\theta_{S1} & -\rho_2 V_{P2}(1-2sin^2\theta_{S2}) & \rho_2 V_{S2} sin2\theta_{S2} \end{pmatrix} \tag{2.41}$$

Considering the reflection coefficients, $\grave{\mathrm{P}}\acute{\mathrm{P}} = R_{PP}$, $\grave{\mathrm{S}}\acute{\mathrm{P}} = R_{SP}$, $\grave{\mathrm{P}}\acute{\mathrm{S}} = R_{PS}$ and $\grave{\mathrm{S}}\acute{\mathrm{S}} = R_{SS}$. From equation 2.39, the explicit solutions for the reflection coefficients is defined by equation A.6 (R_{PP}), equation A.7 (R_{SP}), equation A.8 (R_{PS}) and equation A.9 (R_{SS}). These solutions can be found in appendix section A.4.

Aki and Richards (1980) shows how the Zoeppritz equations can be written in approxi-

mated forms. Assuming small layer contrasts the equation for P-P reflection (equation A.6) can be approximated by equation 2.42. Here, the mean P-wave angle θ is approximated as θ_1, the P-wave angle of incidence (modified Aki and Richards (1980).

$$R_{PP}(\theta) \approx \frac{1}{2}\left(\frac{\Delta V_P}{\bar{V_P}} + \frac{\Delta\rho}{\bar{\rho}}\right) + \left[\frac{1}{2}\frac{\Delta V_P}{\bar{V_P}} - 2\frac{\bar{V_S}^2}{\bar{V_P}^2}\left(2\frac{\Delta V_S}{\bar{V_S}} + \frac{\Delta\rho}{\bar{\rho}}\right)\right] sin^2\theta + \frac{1}{2}\frac{\Delta V_P}{\bar{V_P}}(tan^2\theta - sin^2\theta) \tag{2.42}$$

Further, equation 2.42 can be simplified to equation 2.43.

$$R_{PP}(\theta) \approx R_0 + Gsin^2\theta + C(tan^2\theta - sin^2\theta) \tag{2.43}$$

Where R_0 represents the reflection coefficient for zero incidence (intercept), G the gradient and C the curvature.

$$R_0 = \frac{1}{2}\left(\frac{\Delta V_P}{\bar{V_p}} + \frac{\Delta\rho}{\bar{\rho}}\right) \tag{2.44}$$

$$G = \left[\frac{1}{2}\frac{\Delta V_P}{\bar{V_P}} - 2\frac{\bar{V_S}^2}{\bar{V_P}^2}\left(2\frac{\Delta V_S}{\bar{V_S}} + \frac{\Delta\rho}{\bar{\rho}}\right)\right] \tag{2.45}$$

$$C = \frac{1}{2}\frac{\Delta V_P}{\bar{V_P}} \tag{2.46}$$

Chapter 3

Method

3.1 Chemical classification model

Figure 3.1 shows the chemical classification model used for correlation between mineral compositon and silica content for igneous rocks. The model only represents an approximation of a typical mineral composition for igneous rocks based on a certain silica content, and there are of course individual variations in composition for real occuring rocks. The approximated content of mineral phases is determined by estimating their volume fractions from the model corresponding to silica content, for further use in calculations. In order to determine the mineral fractions, the model was first digitalized in Matlab, resulting in x- and y-pairs for each separate line separating the phases. Here, the x-axis corresponds to the wt% of silica, and the y-axis corresponds to the vol% of minerals. Further, these pairs were interpolated in order to obtain a grid with corresponding y-values for each x-value for a interval of 0.5 wt% silica. From this, the fractions of the solid mineral phases were calculated for the same interval, ranging from 40 wt% to 70 wt% silica. The vol% of the phases were already given directly from the model, so they only needed to be normalized in fractions of one.

3.2 Calculation of elastic bounds and velocity bounds

In order to perform calculations of the elastic bounds, properties were assumed for the constituent mineral phases. They are referred to as mineral phases because there are usually

Figure 3.1: Chemical classification model for igneous rocks, modified version of "Physical Properties of Rocks" figure 1.2 (Schön, 2015a)

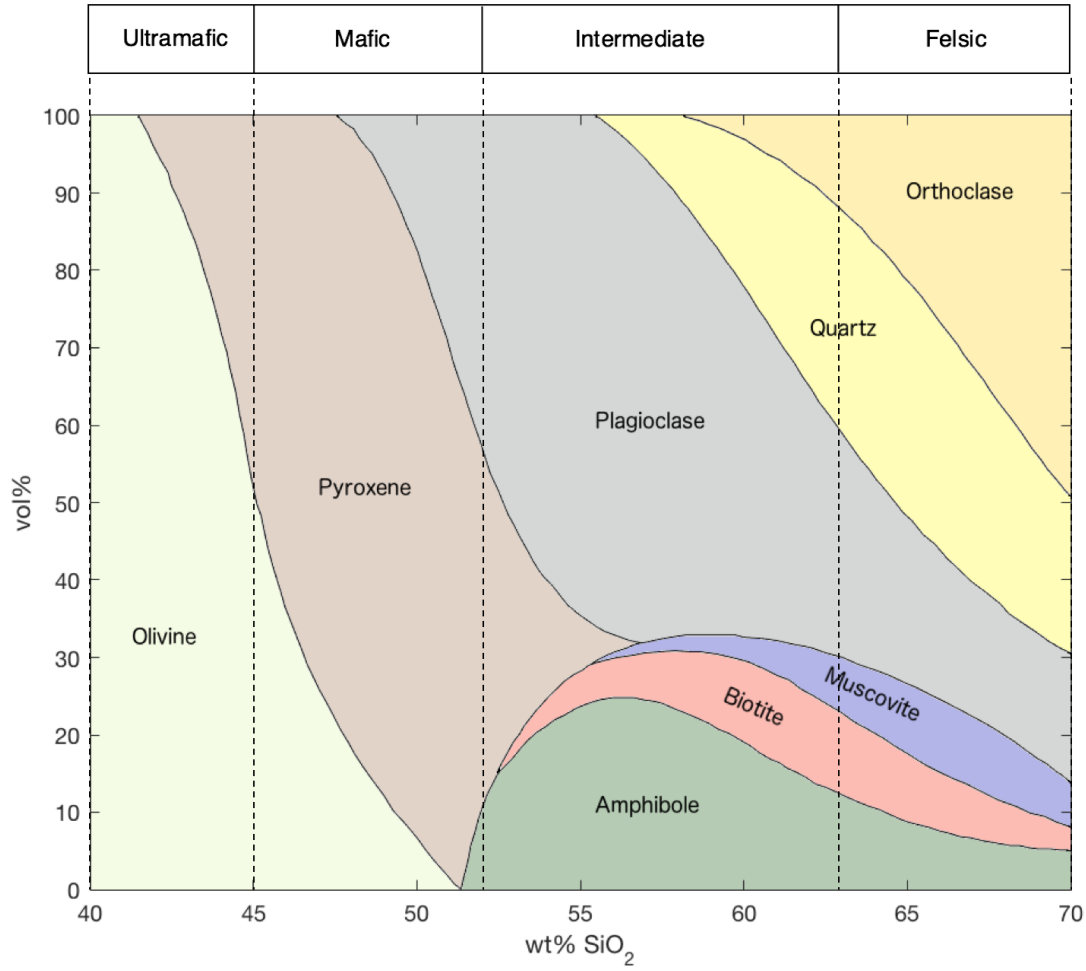

several subgroups of minerals within each of these groups. For calculation of the Hashin-Shtrikman bounds, the properties of interest includes the bulk modulus, shear modulus and density. Properties were exctracted from compilations in two different textbooks; (Schön, 2015a) Table 6.2 and (Mavko et al., 2009) table A.4.1, measured at standard temperature and pressure conditions. A detailed view of these references is shown in appendix A.2. For most of the mineral phases, there was a spreading in the values of the properties, meaning that several different values were given for each of those phases. For these cases, average mineral properties were computed using arithmetic average. Table 3.1 shows the values used in calculations for each mineral phase. By using this approximation, these properties may not be a reliable average for the natural occurence of minerals.

Table 3.1: Elastic properties and density of the phases used in calculations. Data extracted from compilations in (Schön, 2015a) Table 6.2 and (Mavko et al., 2009) table A.4.1

	Bulk modulus (GPa)	**Shear modulus** (GPa)	**Density** (kg/m^3)
Amphibole	87	43	3124
Biotite	50.6	27.3	3050
Muscovite	52.1	31.6	2790
Olivine	129.8	81.8	3321
Pyroxene	102.7	60.4	3285
Plagioclase	71.5	31.7	2663
Quartz	37.2	44.4	2650
Orthoclase	46.8	27.3	2570

The fluid to fill the pore space was assumed to be brine with a salinity of 35 000 ppm, because brine is the most common pore fluid for subsurface rocks. Using the method of Batzle and Wang (Batzle and Wang, 1992), and considering standard temperature of ($20°C$) and pressure conditions (1 atm $\approx$ 0.1 MPa), the bulk modulus (K_{brine}) and density (ρ_{brine}) of brine was estimated to be 2.36 GPa and 1021 kg/m^3 respectively. The method of Batzle and Wang is described in detail in appendix A.1. It is known that the shear modulus of a fluid such as brine, is equal to zero.

Calculations of the elastic bounds were performed using the bulk modulus, shear modulus

and density of the constituents, as well as their mineral fractions for the corresponding range of wt% silica. The elastic bounds were also calculated for all porosities, even though igneous rocks commonly have very low porosities. For calculation of the elastic bounds, equation 2.10 and 2.11 were applied for the composite consisting of solid mineral phases and brine. This resulted in 3D models showing the bounds of the elastic moduli as a function of both silica content and porosity. Further, the corresponding P- and S-wave velocity bounds were computed from the elastic bounds applying equations 2.15 and 2.16 respectively. For the calculations of the velocity bounds, a weighted density average for the composite (ρ_{bulk}) was estimated from the mineral fractions as a function of wt% of silica and porosity (equation 2.14).

A Hashin-Shtrikman average for the P- and S-wave velocity bounds was also computed by applying equations 2.17 and 2.18.

For some cases of use, it was more convenient to apply the data it in terms of approximated values and not ranges for the different classes. Then average silica content was used, shown in table 3.2.

Table 3.2: Minimum, maximum and average values for wt% SiO_2 and average solid density for the classifications

Classification	**Min. wt% SiO_2**	**Max. wt% SiO_2**	**Avg. wt% SiO_2**	**Avg. ρ_{solid} (kg/m^3)**
Felsic	63	70	66.5	2709
Intermediate	52	63	57.5	2795
Mafic	45	52	48.5	3261
Ultramafic	40	45	42.5	3299

3.3 Corrections and assumptions for velocity data

In order to investigate how these theoretical Hashin-Shtrikman velocity bounds relate to the measured velocities for real occuring igneous rocks, velocity data from igneous rock samples were plotted into the bounds. P-wave velocities for basalt was extracted from Matthews (1978), other velocity data from Birch (1961) (for P-waves) and Simmons (1964) (for S-waves). The data for basalt was collected from core samples for a single drill hole. For the

velocity data for all other rock samples than basalt, the data points are mean velocity and density values calculated from 2-3 individual measurements for rock samples from certain locations, meaning that each data points represents a unique location. The locations represents a wide range of different geographical areas from around the globe.

Assuming the bounds for the corresponding range of silica content for the different classifications (as shown in table 3.2), 2D models were obtained, showing the P- and S-wave velocity bounds as a function of porosity (resulting in double upper and lower bounds based on maximum and minimum silica content for each classification). Because the specific silica content of the samples are not given, their silica content is assumed to plot in between the minimum and maximum value of silica content. For example for the granite velocitiy data, a silica content in between 63-70 wt% is assumed. Becuase the model is limited to the interval of 40-70 wt% silica, there may be felsic samples containing more than 70 wt% silica and ultramafic samples containing less than 40 wt%.

For the cases where porosity was not given (P- and S- wave velocities from Birch (1961) and Simmons (1964) respecitvely), porosity was estimated from their given bulk densities, based on the estimated solid density for the average wt% SiO2 for each class (equation 2.30). Also, for the P-wave velocity data (Birch, 1961) the measured velocities are only given for a interval from 1 MPa ($\approx$ 10 atm) up to 1000 MPa ($\approx$ 10 000 atm). Because the seismic velocity generally increases quickly with increase from low to moderate pressures due to compaction, it is necessary to correct for this to atmospheric conditions. Using logarithmic interpolation in Excel, these velocities were interpolated to 0.1 MPa ($\approx$ 1 atm) in order to fit with the assumption of standard pressure conditions.

3.4 Application of the self-consistent approximation

In order to estimate how the elastic properties of rocks are affected by variations in pore geometries, the self consistent approximation was applied for the case of both spherical and penny-shaped inclusions, as well as an equal (50-50%) combination of these. Three cases of ratios for penny shaped cracks were considered; $\alpha = 0.1$, $\alpha = 0.01$ and $\alpha = 0.001$. In theory, penny shaped pores with an aspect ratio of $\alpha = 1$ can be considered as spherical pores.

The inclusions were assumed to be pore space filled with brine with the same properties as specified in section 3.2. The elastic properties were estimated by application of the coupled equations 2.34 and 2.35 for the bulk modulus and the shear modulus respectively. For the solid bulk and shear modulus, the result from Hashin-Shtrikman bounds for zero porosity were applied. Initial guesses were made for the effective elastic moduli K^*_{SC} and G^*_{SC} based on the Voigt average, and the coupled equations were solved iteratively by applying the $fsolve$ function in Matlab. Estimations were made as a function of both silica content and porosity ranging from $\phi = 0$ to $\phi = 0.1$, resulting in a 3D-model. From this model, effective velocities were also estimated.

3.5 Thermal and electrical properties

The thermal and electrical properties of the composite were estimated in terms of thermal conductivity and electrical conductivity. Properties were assumed for the mineral phases based on measurements from Olhoeft (1981) (Electrical conductivity) and compilation extracted from Schön (2015b) table 9.2 (Thermal conductivity). As for the elastic properties, spreading in the values occured for these properties as well for some of the phases. In order to obtain a single value of the properties for each phase, arithmetic averages were calculated and applied in the calculations. For thermal conductivity, the Voigt and Reuss upper and lower bounds as a function of porosity were calculated by applying equations 2.23 and 2.24 respectively. Table 3.3 shows the properties of the individual phases used in calculations.

For pure water (H_2O) at $20°C$, the thermal conductivity is estimated to be approximately 0.6 W/mK (Schön, 2015b). This was the pore fluid used in calculation of the Voigt and Reuss bounds. The electrical conductivity of pure water is estimated to be $5.5 \cdot 10^{-6}$ S/m (Olhoeft, 1981).

Table 3.3: Thermal conductivity and electrical conductivity of the phases used in calculations. Data extracted from Olhoeft (1981) (Electrical conductivity) and Schön (2015b) table 9.2 (Thermal conductivity)

	Thermal conductivity (W/mK)	**Electrical conductivity** (S/m)
Amphibole	2.88	$2.1{\cdot}10^{-11}$
Biotite	1.45	$1.2{\cdot}10^{-11}$
Muscovite	2.3	$4.6{\cdot}10^{-13}$
Olivine	5.36	$3.5{\cdot}10^{-10}$
Pyroxene	4.57	$2.1{\cdot}10^{-11}$
Plagioclase	2.2	$2.1{\cdot}10^{-9}$
Quartz	6.5	$5{\cdot}10^{-15}$
Orthoclase	2.36	$6.9{\cdot}10^{-13}$

3.6 Reflectivity modelling

In order to model the theoretical reflectivity of the basement, simple half-space single interface models were considered as realistic cases of basement with an overlying sedimentary half-space. Both sand and clay were considered for the overburden sedimentary layer. Properties for sand were considered from the elastic properties of quartz, K_{qtz} = 37 GPa and G_{qtz} = 44 GPa (Carmichael, 1989). The density of sand is given to be ρ_{qtz} = 2.65 g/cc. Vernik and Kachanov (2010) evaluates the elastic properties of clay using the shale model to be c_{33} = 33.4 GPa and c_{44} = 8.5 GPa. They also estimate the average clay density to be ρ_{clay} = 2.73 g/cc. These are the properties used for calculation of velocities. Velocities for sand were calculated from equations 2.12 and 2.13 while velocities for clay were calculated from equations 2.19 and 2.20.

For the basement, the scenarios considered are the four classifications; felsic, intermediate, mafic and ultramafic. Velocity values for the average wt% SiO_2 of the four classifications were considered, for the cases of $\phi = 0$, $\phi = 0.05$ and $\phi = 0.1$. Average silica values for the classes are shown in table 3.2. The velocities were calculated based on the estimation of elastic moduli by applying the self-consistent approximation for a combination of spherical

and penny shaped pores with an aspect ratio of $\alpha = 0.01$. The reason for this is because specific velocities (and not ranges) needs to be assumed, and this case has shown to be an approximate average estimate based on comparison with velocity data.

Reflection coefficients were calculated for the theoretical interfaces as a function of incident angle θ by applying the Zoeppritz equations. Both P-P, P-S and S-S reflection were considered, and the reflection coefficients R_{PP}, R_{PS} and R_{SS} were calculated from equation 2.39. Intercept-gradient and intercept-curvature plots were produced from the parameters R_0 (intercept), G (gradient) and C (curvature) from equations 2.44, 2.45 and 2.37 respectively.

Because the oceanic crust is mainly made up of basalt, the velocity model for an average mafic composition was assumed to be a good estimate for the oceanic crust. Correspondingly the velocity model for felsic average was assumed to be a good estimate for the continental crust, which is mainly made up of granite. The idea was to compare the modelled theoretical reflectivity of the theoretical half-space models to real seismic data. It is important to emphasize that the modelling considers the reflection coefficients of the interfaces, while the strength of the reflection amplitudes are considered when studying the seismic. Large reflection coefficient yields high amplitudes, and small reflection coefficients yields low amplitudes.

Seismic data from offshore Norway were given from the NTNU-NPD-SCHLUMBERGER Petrel ready database, containing seismic lines from the Norwegian Sea and Barents Sea. Previous interpretations of the COB along the offshore Norwegian coast includes Olesen et al. (2007) and Marcussen et al. (2009), and their figures gives an idea about approximately where the boundary is located. Figure 3.2 shows the approximate placement COB offshore Norway, extracted from Marcussen et al. (2009). Based on this observation, the seismic line NPD-NH-79_NPD-TR02-74-NH-1-_FM_GC was selected for interpretation, because it has a long extension around where the COB should be located. The seismic section was interpreted, and the basement reflector was studied in order to try to identify the COB. Wells that penetrates basement rocks are in general rare, and the well data available were to shallow in depth to be helpful in the determination of the COB. Because the oceanic crust generally is a low thermal conductor, the sediments above are less likely to gain maturity for generation of hydrocarbons (D.V. Reddy, 2013). This explains why most wells are drilled on continental shelf.

Figure 3.2: An illustration showing the approximate location of the COB offshore Norway. Figure courtesy: Marcussen et al. (2009)

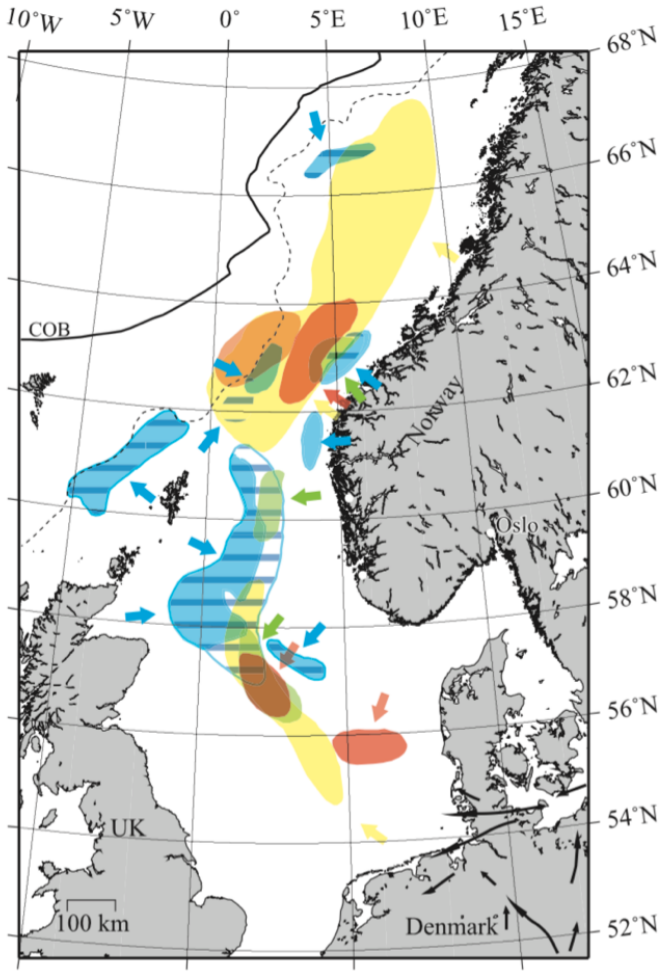

Chapter 4

Results

4.1 Theoretical Hashin-Shtrikman bounds

The resulting 3D models after calculation of the Hashin-Shtrikman bounds for the elastic moduli and velocities are shown in appendix A.3. Figure A.1 shows the 3d model of the bulk and shear moduli as a function of both porosity and silica content. The figure shows a clear trend of increasing values of the elastic moduli for decreasing porosities as well as decreasing silica content. The values for the bulk modulus are generally higher than the values for the shear modulus. The lower bound for the shear modulus is zero for all porosities except zero (solid rock).

Both the bulk and the shear modulus shows a particularly steep increase in the modulus for a decrease of silica content in the interval of approximately 52 to 40 wt% corresponding to mafic and ultramafic, than for the interval of approximately 70 to 52 wt% corresponding to felsic and intermediate. The shear modulus is relatively stable for the felsic and intermediate intervals given zero porosity, while the bulk modulus is generally increasing steadily for every decrease in silica content, even though the slope is significantly steeper for low silica content.

Figure A.2 shows the estimated P- and S-wave velocitiy bounds calculated from the elastic bounds of the bulk and shear moduli. It is clear that the velocity bounds follows the same trend as the bounds for the elastic moduli shown in figure A.1; The velocity bounds generally decreases with both porosity and silica content, and it is also seen here that the velocities decreases at a steeper rate for ultramafic and mafic rocks than for intermediate and felsic

rocks for zero porosity. This observation is better illustrated in figure 4.1, which shows the velocity and density distributions due to silica content for zero porosity. There is a strong correlation between the S-wave velocity and the shear moduli, and the P-wave velocity shows a stronger dependance of the bulk moduli than the shear moduli.

The transition between intermediate and mafic represents the most distinct change in both the velocity and density distributions, as the differences between felsic and intermediate are not too significant. This trend is stronger for the S-wave velocity and density than for P-wave velocity. From the 3D model, it is also observed that the bounds are broader (the range of the moduli is greater) for low silica content (ultramafic) than for high silica content (felsic), which might indicate that there is a higher variation in the velocities for the rocks with less silica content. For zero porosities, the values for the upper and lower bounds are identical.

Figure 4.2 shows a contour plot of the P-wave Hashin-Shtrikman average, as well as the estimated density as a function of porosity and silica content. A porosity range of 0-20 % is chosen based on the fact that real occuring igneous rocks very rarely has a porosity higher than 20 %. The S-wave Hashin-Shtrikman average does not represent an appropriate estimate, and is therefore not included. This matter will be further discussed in section 5.2. This contour plot enhances the earlier observation that the density increases significantly in the transition between intermediate and mafic (around 52 wt% silica). It can also be observed that the density increases quite uniformly with decreasing porosity, while the P-wave velocity shows a much steeper increase for very small porosities (0-5%) than for larger porosities (5-20%).

Figure 4.1: Distribution of the modelled P-wave velocities, S-wave velocities and densities for zero porosity

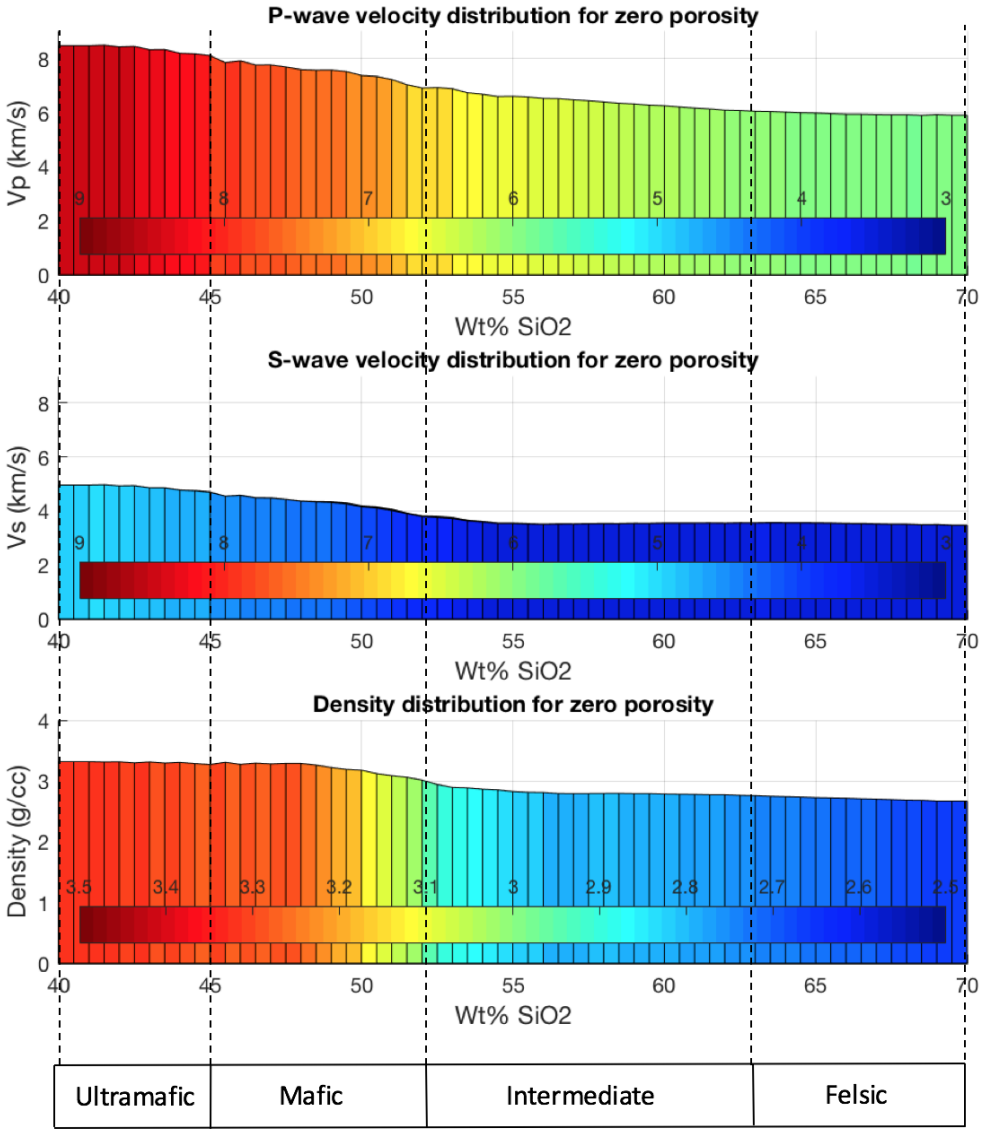

Figure 4.2: Contour plot for the P-wave Hashin-Shtrikman average velocity and the density as a function of wt% silica and porosity ranging from 0-20%.

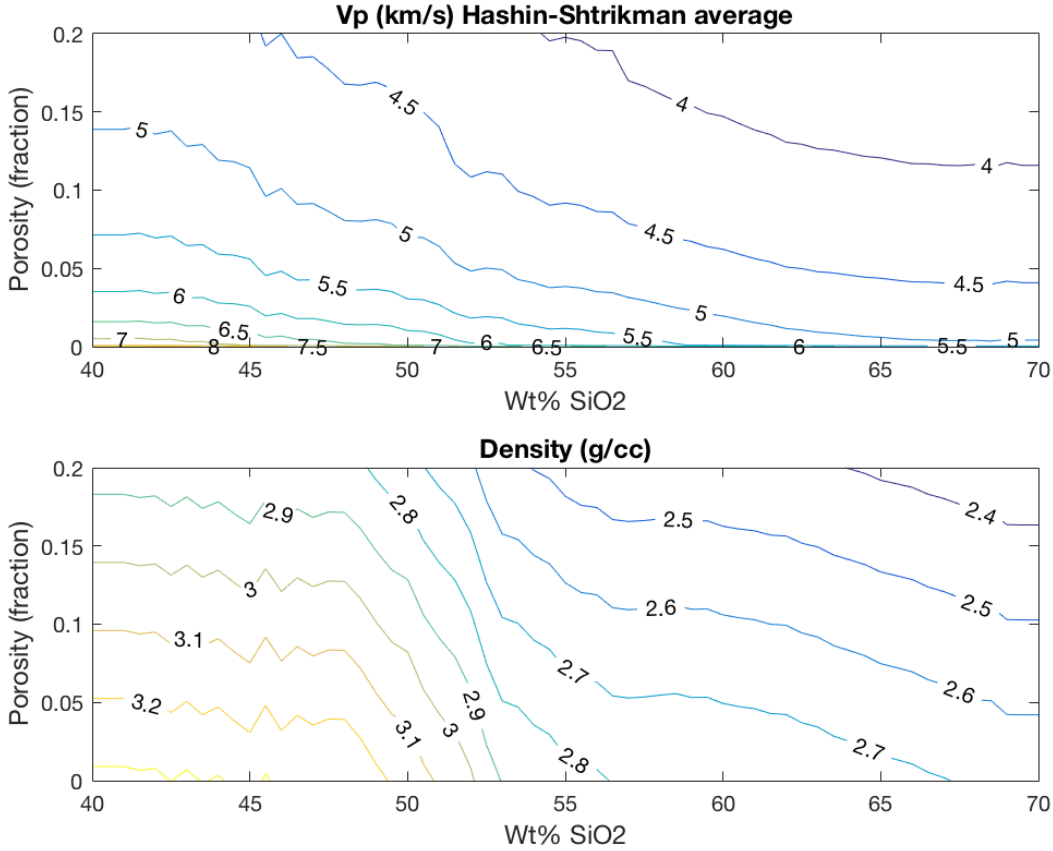

4.2 Model with core sample measurements

Figures 4.3, 4.4, 4.5 and 4.6 shows how measured velocities from core sample measurements plots into the calculated Hashin-Shtrikman velocity bounds for felsic, intermediate, mafic and ultramafic rocks respectively. A Hashin-Shrikman average velocity trend is also shown in red. The double upper and lower bounds represents the range of silica associated with the categorization, whereas the higher upper and lower bound represents the minimum silica content for the categorization, and the lower upper and lower bound represents the maximum silica content. For the S-wave, the lower bounds are equal to zero for all porosities except zero porosity, as for the shear modulus. The lower P-wave velocity bounds are nearly similar for all cases, while the upper bounds shows the greatest differences. For intermediate and mafic rocks these upper bounds varies significantly, while for felsic and ultramafic the differences are less significant, but still larger than for the lower bounds.

For some cases, the porosities of the samples calculated from their corresponding bulk densities as well as the estimated solid densities for each categorization, resulted in negative porosities. This, as a result of higher bulk density of the rock sample than the estimated average solid density for that classification. Negative porosities are not possible, and therefore these porosities were set as zero. This will be further discussed in section 5.3.

For the felsic categorization (figure 4.3), the rock samples, including granite, monzonite, granodiorite, tonalite and diorite are all intrusive. The figure shows a great variation of P-wave velocities distributed along the whole velocity spectrum (from approximately 3-6 km/s), especially for granite. Some samples even plot just outside the velocity bounds. However, the average velocity of the samples seem likely to be situated approximately around the estimated Hashin-Shtrikman average of the bounds. The estimated porosities are generally quite low (less than 10%). The S-wave velocities are more uniform (around 3 km/s), but contain fewer samples than for the P-wave. They are generally distributed close to the upper velocity bounds.

For intermediate (figure 4.4) only a few samples are represented. Both anorthosite and syenite are intrusive rocks. The anorthosite samples plot in between the minimum and the maximum upper bounds for both the P-wave and the S-wave, but for the P-wave the samples

Figure 4.3: Velocity bounds for felsic rocks with velocity data (SiO2 = 63-70 wt%). Data courtesy: Birch (1961) (P-wave velocities); Simmons (1964) (S-wave velocities).

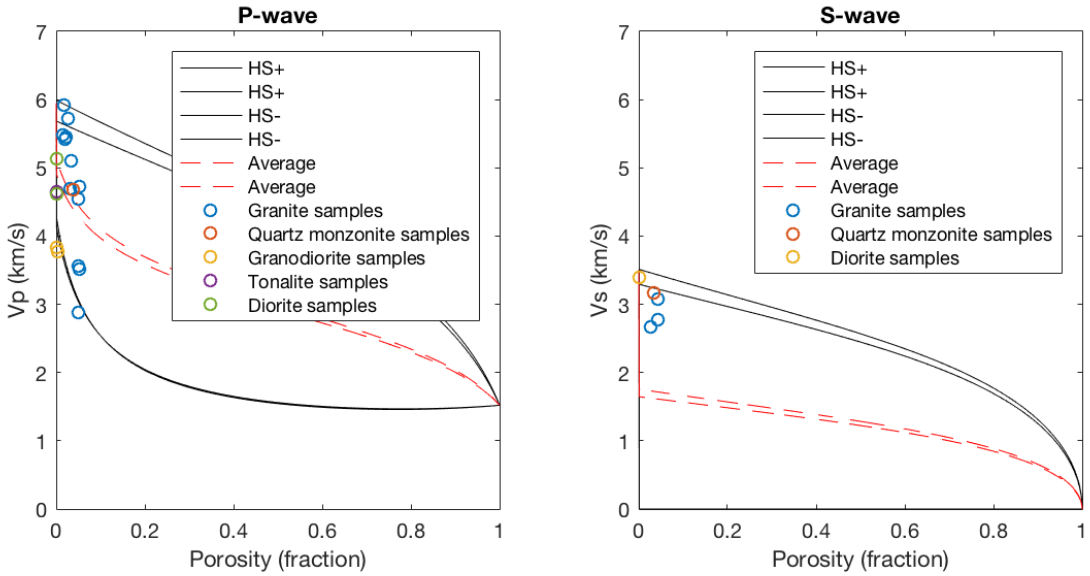

also plot very close to the Hashin-Shtrikman average, because the bounds are very narrow for very low porosities (only a few %). There is a large spreading between the maximum and the minimum upper bound for the P-wave velocity.

For mafic rocks (figure 4.5) there are an abundance of basalt samples for the P-wave velocity. They plot very well along the Hashin-Shtrikman average line, with estimated porosities varying from 0 to almost 40%. Basalt is an extrutive mafic rock, whereas the intrusive equivalent is gabbro. The plot shows a generally higher velocity for gabbro (generally close to the minimum upper bound) than for basalt. Diabase is texturally in between basalt and gabbro (in between intrusive and extrusive). The velocity of the diabase samples are generally plotted quite close to the gabbro samples. The porosity of the diabase and gabbro samples are generally estimated to be around 20%, which is quite high for igneous rocks, but the reliability of the porosity estimation of the samples will be discussed later.

For ultramafic (figure 4.6) the samples generally plots close to the Hashin-Shtrikman average for the P-wave, and closer to the upper bounds for the S-wave. Rock samples include dunite, jadeite, pyroxenite, bonzitite and harzburgite. Dunite is an intrusive ultramafic rock also known as olivinite, almost entirely made up of olivine, meaning that its silica content

Figure 4.4: Velocity bounds for intermediate rocks with velocity data (SiO2 = 52-63 wt%). Data courtesy: Birch (1961) (P-wave velocities); Simmons (1964) (S-wave velocities).

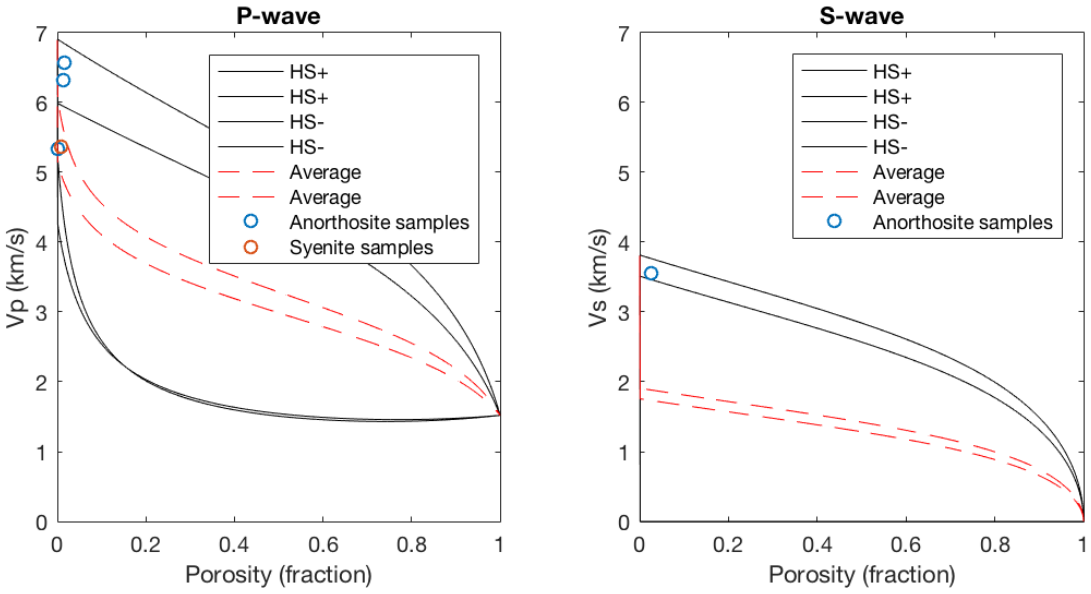

Figure 4.5: Velocity bounds for mafic rocks with velocity data (SiO2 = 45-52 wt%). Data courtesy: Matthews (1978) (basalt P-wave velocities); Birch (1961) (other P-wave velocities); Simmons (1964) (S-wave velocities).

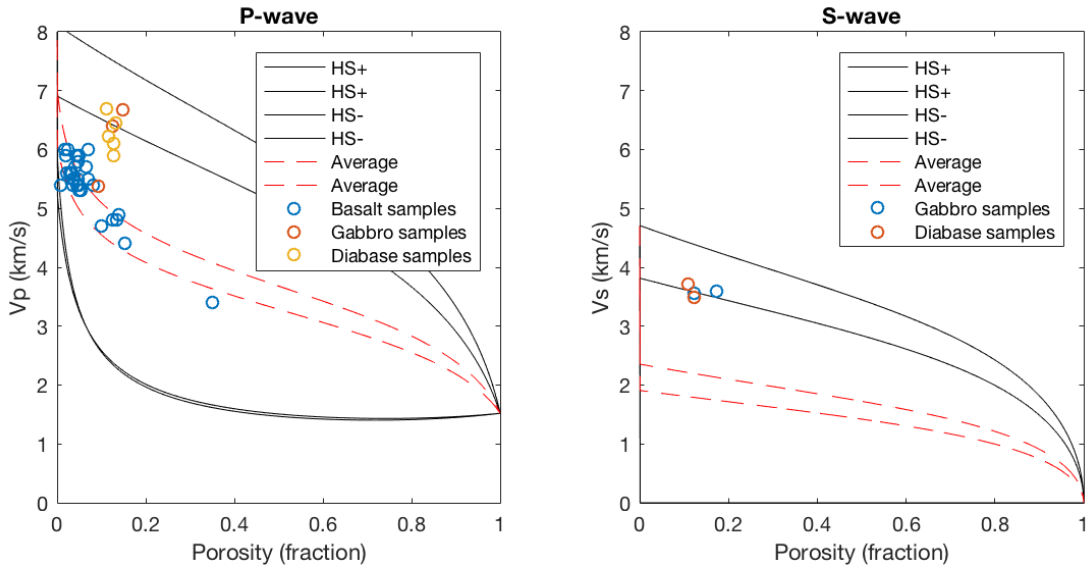

Figure 4.6: Velocity bounds for ultramafic rocks with velocity data (SiO2 = 40-45 wt%). Data courtesy Birch (1961) (P-wave velocities); Simmons (1964) (S-wave velocities).

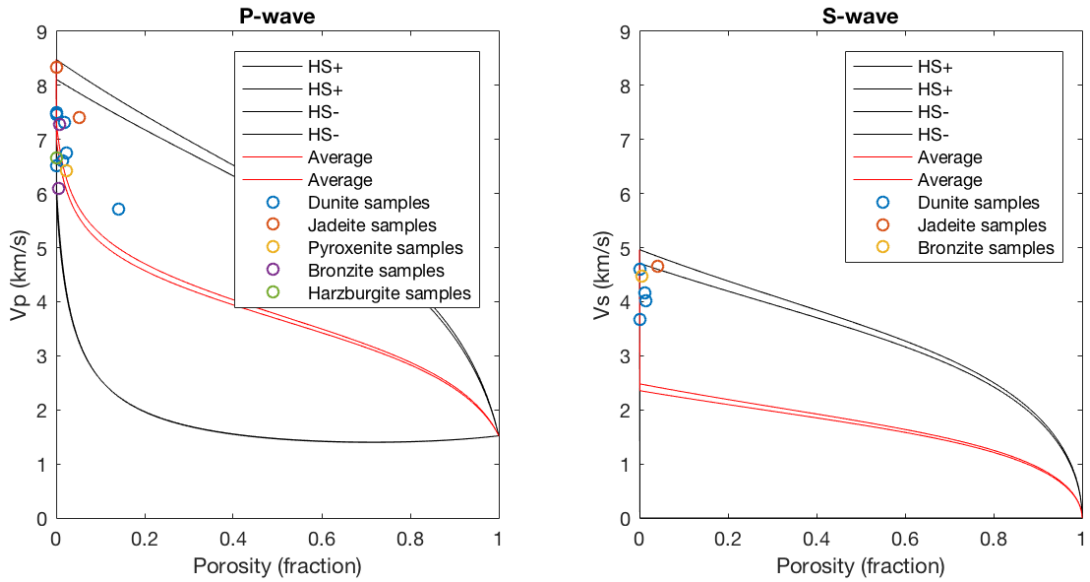

should be close to 40 wt% with reference to the model. Pyroxenite is a rock consisting essentially of minerals in the pyroxene group, while jadeite represents a pure pyroxene mineral. Bronzitite is made up of olivine and pyroxene minerals, mostly the pyroxene mineral bronzite, and harzburgite is a variety of peridotite consisting mostly of the pyroxene mineral enstatite and olivine.

4.3 Variations in velocities with increasing stress

Figure 4.7 shows how the measured P-wave velocity is affected by changes in stress conditions for granite, for the same granite samples as shown in figure 4.3 for pressures up to 1000 MPa ($\approx$ 10 000 atm). The figure shows a rapid increase in velocities due to increasing stress for low pressures, and a more slowly increase for higher pressures. This is the normal velocity-stress trend for rocks. The steep increase of velocity for low pressures is due to compaction, which results in closure of fractures and pores that contributes to an increase in bulk density. For higher pressure the rock is already well compacted, so the increase in velocity is less steep with increasing pressure. This plot illustrates why it was necessary to correct the velocity

Figure 4.7: Velocity bounds for average felsic rocks with velocity and pressure data for granites (Wt% SiO2 = 70) with standard temperature conditions. Data courtesy: Birch (1961).

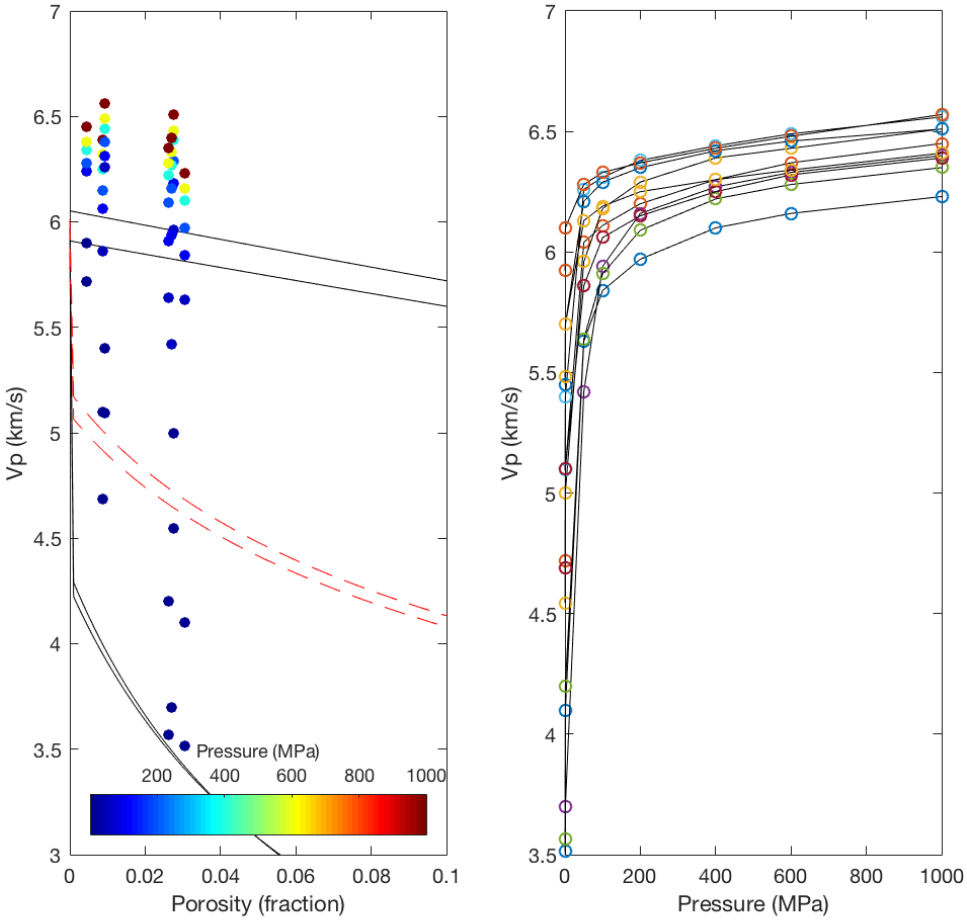

data from 1 MPa (≈ 10 atm) to 0.1 MPa (≈ 1 atm). As the velocity changes quickly for low pressures, the difference in velocity from 10 atm to 1 atm is therefore significant. The S-wave velocity data was already given for standard pressure conditions of 0.1 MPa.

The figure also shows that for the case of high stress conditions (pressure higher than around 200 MPa), the measured samples plots outside of the Hashin-Shtrikman bounds. This may also represent a weakness of the Hashin-Shtrikman bounds, and will be further discussed in section 5.3.

4.4 Variations in pore geometries

Figure 4.8 shows the estimation of the elastic moduli from the self-consistent approximation as a function of porosity. Bulk modulus (figure 4.8a) and shear modulus (figure 4.8b) are shown for a silica content equivavelt to the mafic average (wt% SiO_2 = 48.5). The theoretical Hashin-Shtrikman bounds are also plotted. The plots show the cases of inclusion of only shperical pores, only penny shaped pores or an equal (50-50%) combination of these. Spherical inclusions represents stiff pores, while penny shaped inclusions represents more soft pores, depending on the aspect ratio. Therefore, variations in aspect ratio (α) of the penny shaped pores is also illustrated. For both the cases, the estimates fits well inside the Hashin-Shtrikman bounds. For the case of only spherical inclusions, the moduli lies very close to the upper Hashin-Shtrikman bound, representing the theoretical stiffest possible pores. For the case of only penny shaped pores, the estimated moduli is always lower. For an equal combination of spherical and penny shaped pores, the moduli is somewhat higher than for only penny shaped pores.

From these plots, it is clear that the aspect ratio of the penny shaped pores greatly affects the elastic moduli, given that the differences between $\alpha = 0.1$ (red line), $\alpha = 0.01$ (green line) and $\alpha = 0.001$ (blue line) are significant. The general trend seen from these plots is that the smaller the aspect ratio, the smaller the elastic moduli. Further, it seems like the effect of decreasing aspect ratio is stronger for the shear modulus than for the bulk modulus, as the spreading is definitely larger for the shear modulus. For infinitely small aspect ratio, the estimated moduli would probably lie close to the lower Hashin-Shtrikman bound for both the bulk and the shear modulus.

Figure 4.8: Estimation of bulk and shear modulus by application of the self-consistent approximation for three cases of pore types; spherical pores, penny cracks and an equal combination (50-50%). For the penny cracks, aspect ratios of 0.1, 0.01 and 0.001 were considered. Wt% SiO2=48.5 (mafic average)

(a) Bulk modulus K

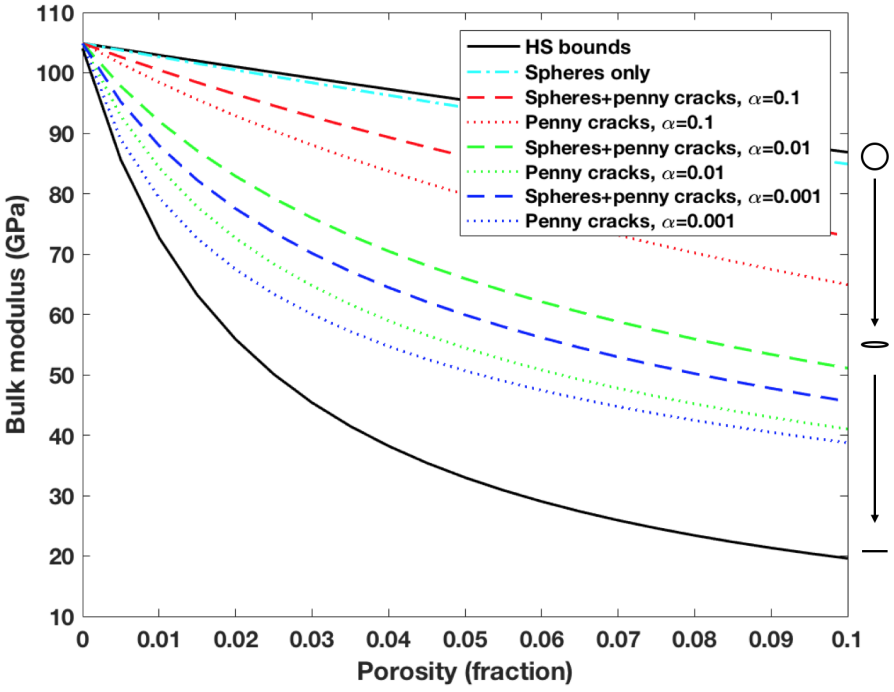

(b) Shear modulus G

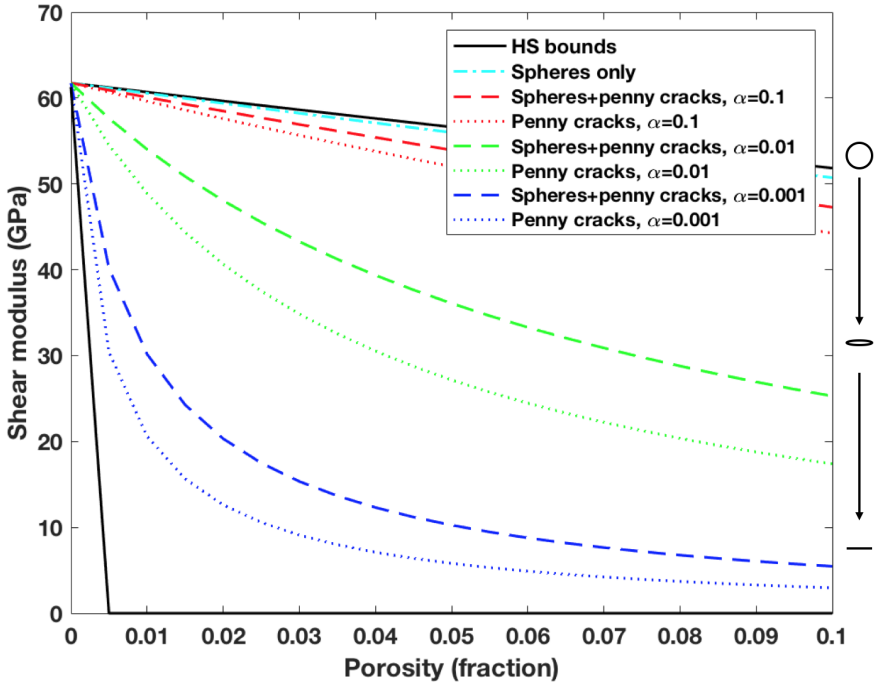

Figure 4.9: Estimation of P-wave velocity by application of the self-consistent approximation for three cases of pore types; spherical pores, penny cracks and an equal combination (50-50%). For the penny cracks, aspect ratios of 0.1, 0.01 and 0.01 were considered. Wt% SiO2=48.5 (mafic average)

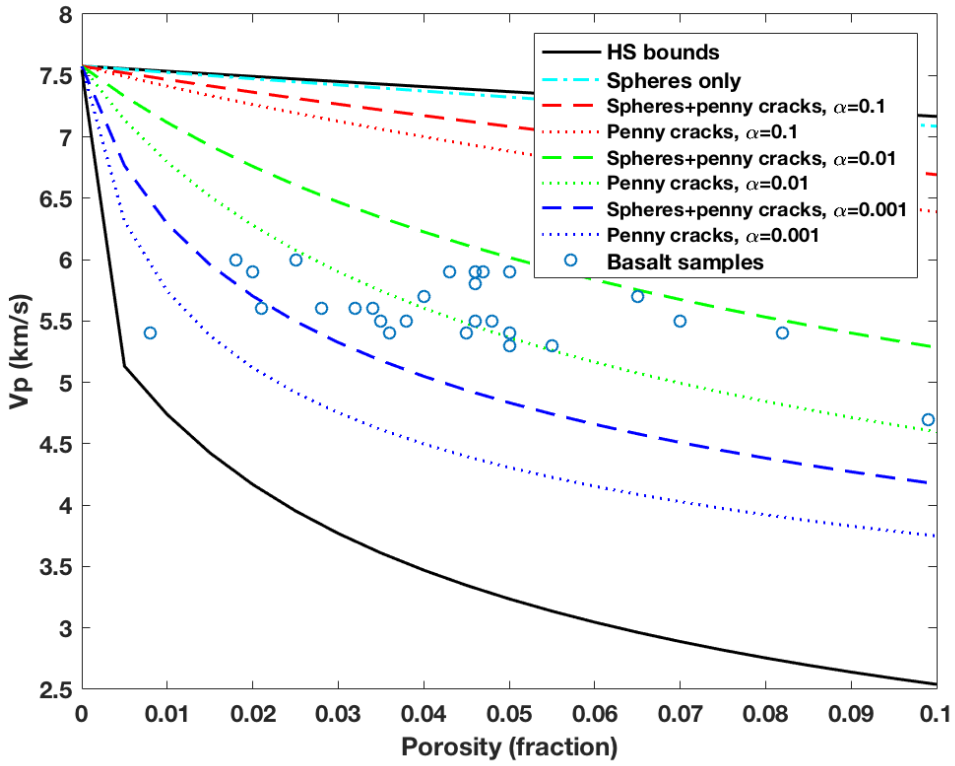

Figure 4.9 shows the application of the self-consistent approximation in terms of velocity, for a silica content equivavelt to mafic average. The velocity was calculated from the bulk and shear moduli shown in figure 4.8a and 4.8b respectively. The Hashin-Shtrikman bounds for velocity are also shown. In order to compare these estimations to real data, velocity data for a variety of basalt samples exctracted from Matthews (1978) are also plotted. As observed from the plot, the samples are mainly situated in the middle of the Hashin-Shtrikman bounds, close to the green dotted line, representing penny cracks with an aspect ratio of 0.01. There are of course variations for the individual samples, which can give us an impression of the stiffness of the pores.

Figure 4.10 shows the distribution of V_p, V_s and density for zero porosity (figure 4.10a), 5% porosity (figure 4.10b) and 10% porosity (figure 4.10c) as a function of silica content from the approximation of spheres + penny cracks with an aspect ratio of $\alpha = 0.01$. As seen from figure 4.8, this can be seen as the green stipled line lying approxamately in the middle of the elastic bounds.

As seen from the plots, the general trend is that the values for both V_p, V_s and density are increasing from high to low SiO_2 content. V_p is increasing quite constantly with decrease of silica content, but the increase appear to be steeper for lower silica content than for higher silica content. For V_s, the values does not change much between 70 and approximately 55 wt% SiO_2, while for SiO_2 content lower than 55 wt% there is a clear increase in velocity for decrease of silica content. Density shows a steep increase around 50 - 55 wt% SiO_2, approximately where intermediate changes to mafic. The density itself appear to be quite stable approximately in the interval of 40 - 50 wt% silica, and the interval 55 - 70 wt%.

For both V_p, V_s and density, the seperation between high silica content (approximately 55-70 wt% silica) and low silica content (approximately 40-55 wt%) is clear. For higher porosities, the values for both the velocities and the densities is smaller, as brine has significantly smaller moduli and density than solid rock. Even though the same trend is still shown, the slope of the increase is smaller for higher porosities.

Figure 4.10: Distribution of the modelled P-wave velocities, S-wave velocities and densities for zero porosity, 5% porosity and 10% porosity as a function of silica content. The pores are a combination (50-50%) of spherical and penny shaped inclusions with an aspect ratio of 0.01.

(a) 0% porosity (b) 5% porosity (c) 10% porosity

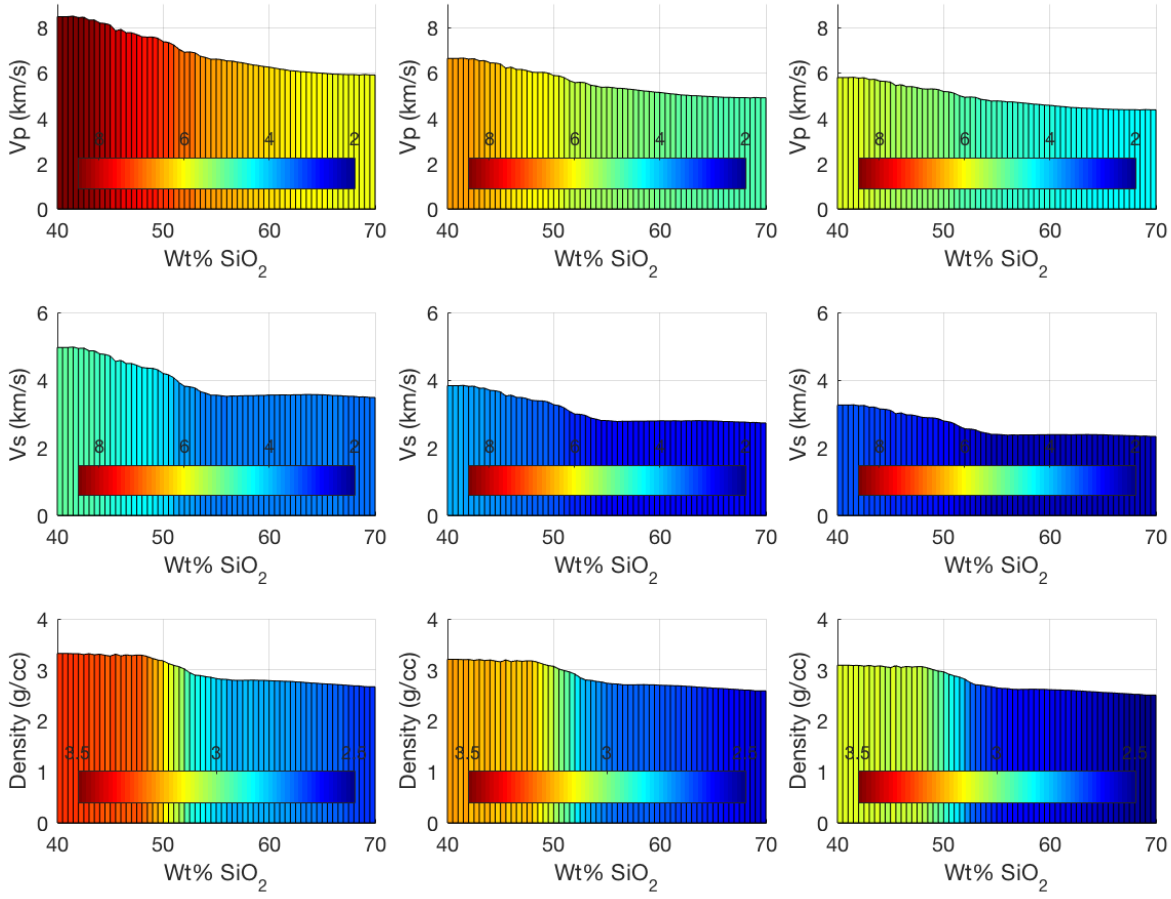

4.5 Distribution of thermal and electrical conductivity

The result after calculation of thermal conductivity and electrical conductivity as a function of silica content for zero porosity is shown in figure 4.11. Unlike the distribution for elastic moduli and velocities, the values for these properties does not show an constantly increasing trend from high to low silica content. For thermal conductivity, the minimum values are observed around 55 wt%, mostly between 50 and 60 wt%. However, for silica content lower than 55 wt%, the distribution shows increasing values for decreasing silica content, with the largest thermal conductivities for ultramafic rocks with the lowest silica content, and the highest content of ferromagnesian minerals.

In contrast to the thermal conductivity, the electrical conductivity shows the largest value where the thermal conductivity shows the minimum value. This is an interesting observation, given that both the thermal conductivity and the electrical conductivity shows the same increasing trend for decreasing silica content for low silica values (from approximately 48-40 wt%) and high silica values (from approximately 70-65 wt%).

The calculation of the Voigt and Reuss bounds for the thermal conductivity as a function of silica content is shown in figure 4.12 for an average mafic composite. The fluid to fill the pore space is pure water, H_2O. The bounds show the same trend as for the elastic properties, the thermal conductivity decreases with increasing porosity.

Figure 4.11: The estimated distribution of thermal and electrical conductivity as a function of silica content for zero porosity

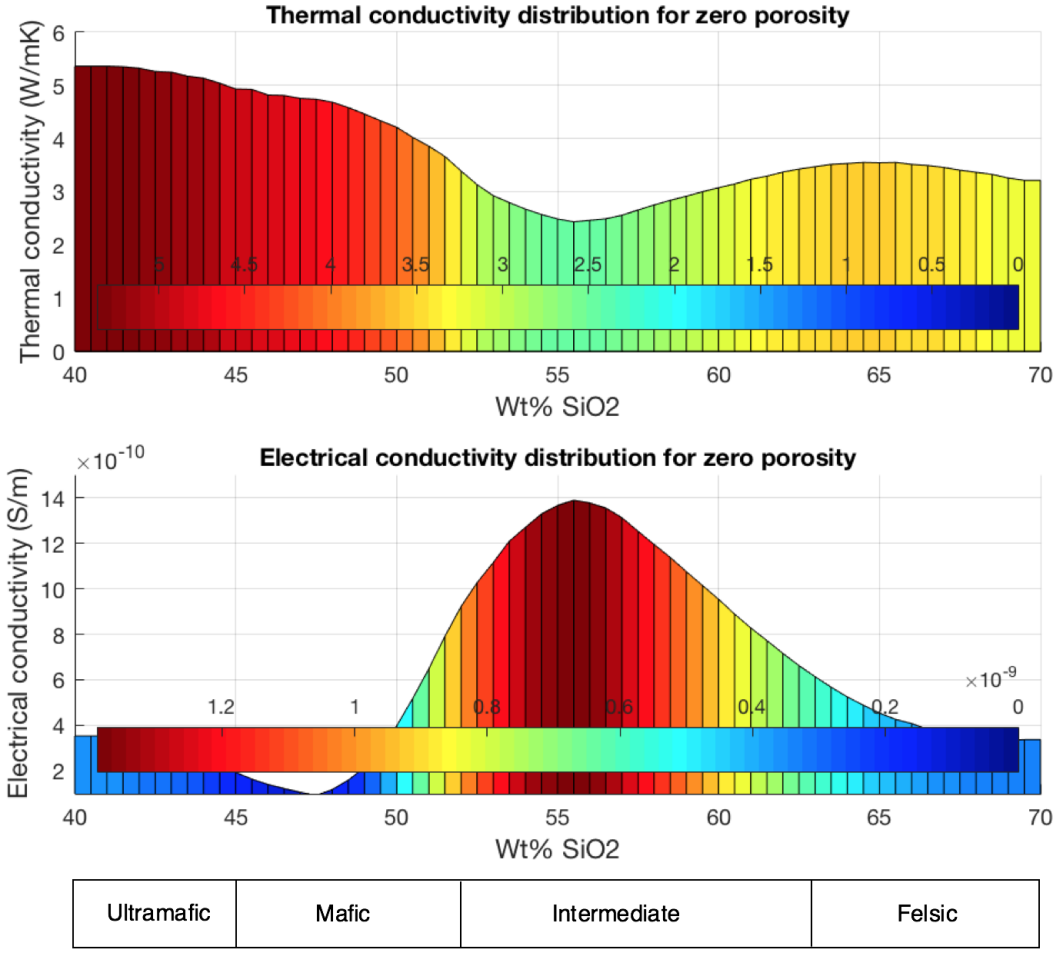

Figure 4.12: Voigt and Reuss bounds for thermal conductivity. Wt% SiO2 = 48.5 (mafic average)

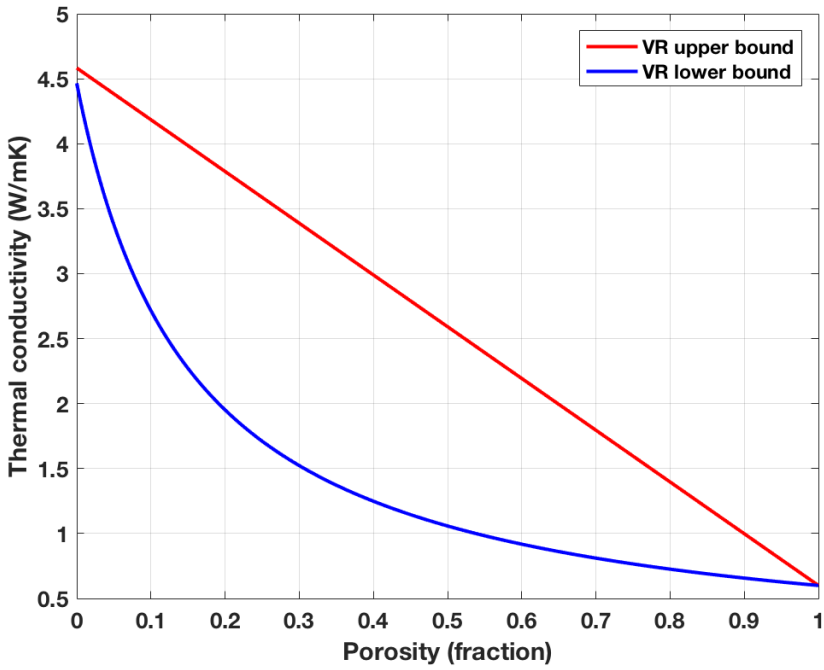

4.6 Vp/Vs ratios and acoustic impedance

Figure 4.13 shows the Vp/Vs ratio versus the acoustic impedance for velocities approximated by the self-consistent approximation, considering a 50-50% combination of spherical and penny shaped pores with an aspect ratio of 0.01. The cases of zero porosity, 5% porosity and 10% porosity were considered. From left to right, each point represents a decrease in silica content by 0.5 wt%, for the interval ranging from 70% to 40% silica. Yellow points represents felsic, green intermediate, red mafic and blue ultramafic.

As seen from the plot, the general trend is that the acoustic impedance decreases with increasing silica content, as well as with increasing porosity. The points are very closely spaced for felsic and ultramafic, and the acoustic impedance only shows a small variation. However, around the transition between intermediate and mafic the points are more spread out, with larger space between them. Intermediate and mafic therefore represents a larger interval of acoustic impedance than felsic and ultramafic. Also, the total interval of acoustic impedance decreases with increasing porosity.

The Vp/Vs ratio generally increases with increasing porosity. The variation of Vp/Vs ratio due to silica content is more complex. Starting to the left with felsic at 70% silica, the Vp/Vs ratio is approximately 1.7 for zero porosity, 1.8 for 5% porosity and 1.88 for 10% porosity. For decreasing silica content, the Vp/Vs ratio is first decreasing, while it changes direction and starts to increase before the transition to intermediate. For intermediate, the Vp/Vs ratio increases quite strongly, reaching a maximum ratio of approximately 1.86 for zero porosity, 1.93 for 5% porosity and 2 for 10% porosity, before it again changes direction and starts to decrease. The Vp/Vs ratio continues to decrease with decreasing silica content for mafic and ultramafic, reaching a final Vp/Vs ratio of 1.7 (same as the starting value) for zero porosity, 1.73 for 5% porosity and 1.77 for 10% porosity. The decrease is much stronger for the case of 10% porosity than for zero porosity.

From the plot, it can also be observed that the change in Vp/Vs ratio for a high-silica composite (before the maximum is reached) is larger for zero porosity than for higher porosities, while the change for a low-silica composite (after the maximum is reached) is smaller for zero porosity than for higher porosities.

Figure 4.13: Vp/Vs ratio versus acoustic impedance for 0% porosity, 5% porosity and 10 % porosity. Velocity were estimated by application of the self-consistent approximation for a 50-50% combination of spherical and penny shaped pores with an aspect ratio of 0.01

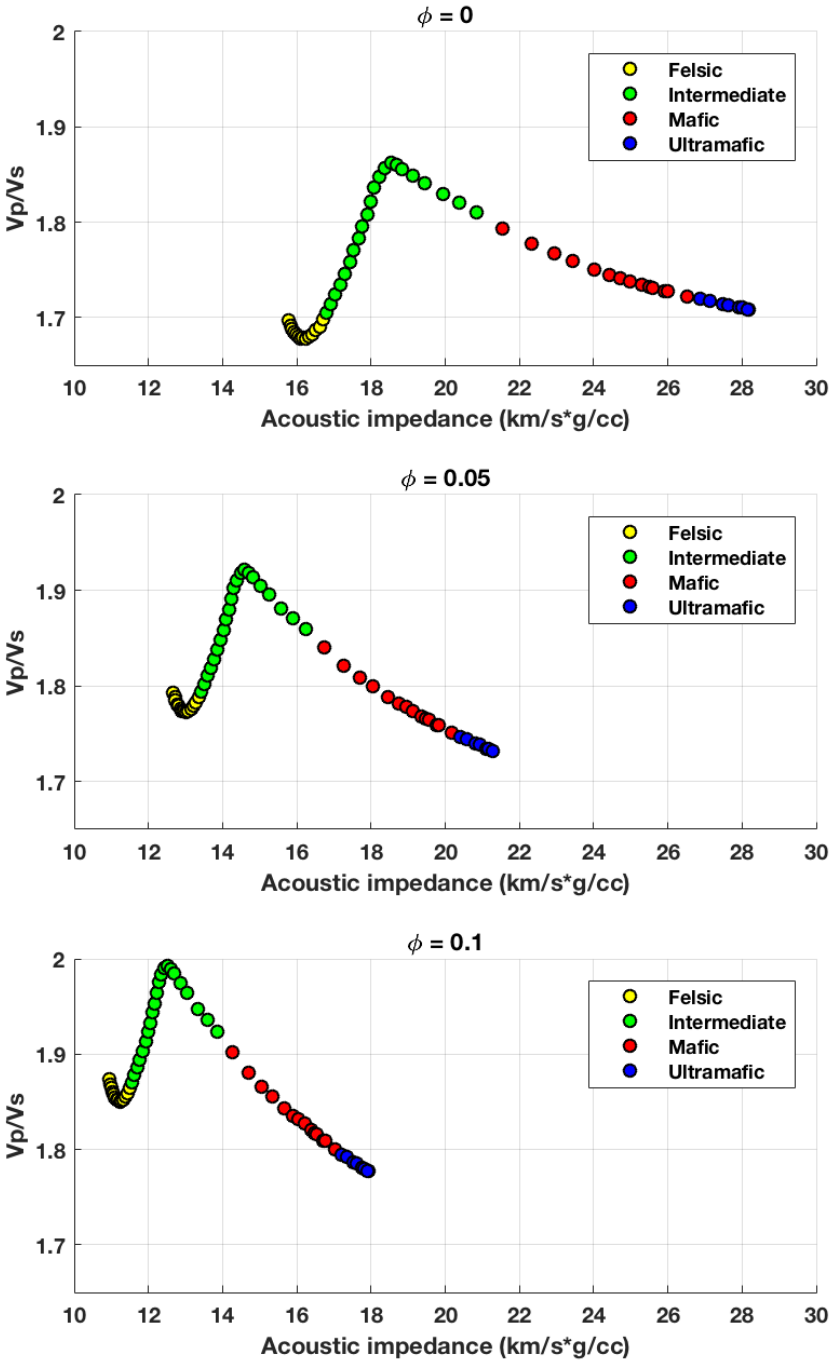

4.7 Half-space single interface models

Figure 4.14: Half-space models showing velocities and densities for the case of sand above basement. The basement represents estimated average values for each of the four classes. The porosity of the sand half-space is constant, $\phi = 0$.

(a) $\phi = 0$

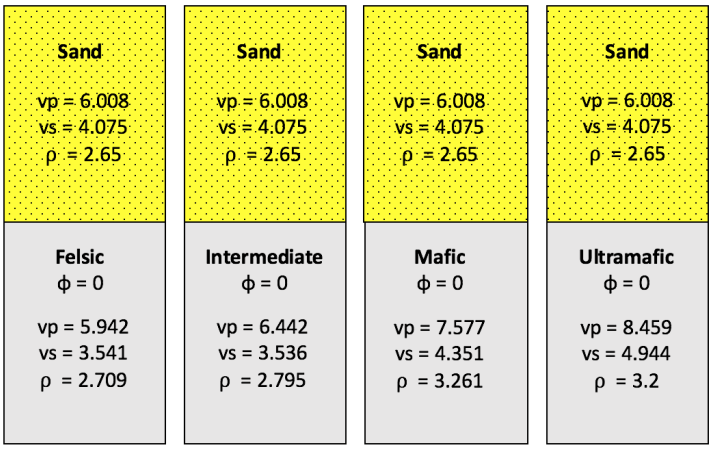

(b) $\phi = 0.05$

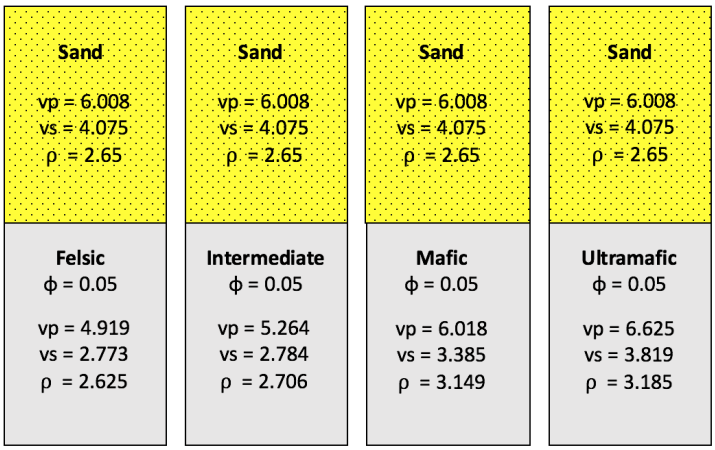

(c) $\phi = 0.1$

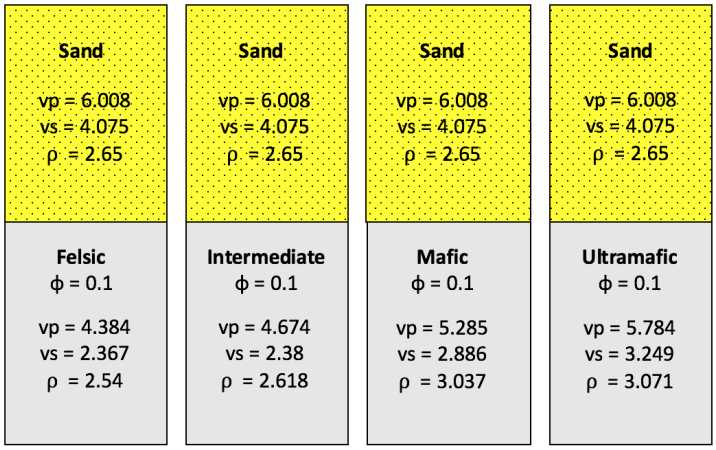

Figure 4.15: Half-space models showing velocities and densities for the case of clay above basement. The basement represents estimated average values for each of the four classes. The porosity of the clay half-space is constant, $\phi = 0$.

(a) $\phi = 0$

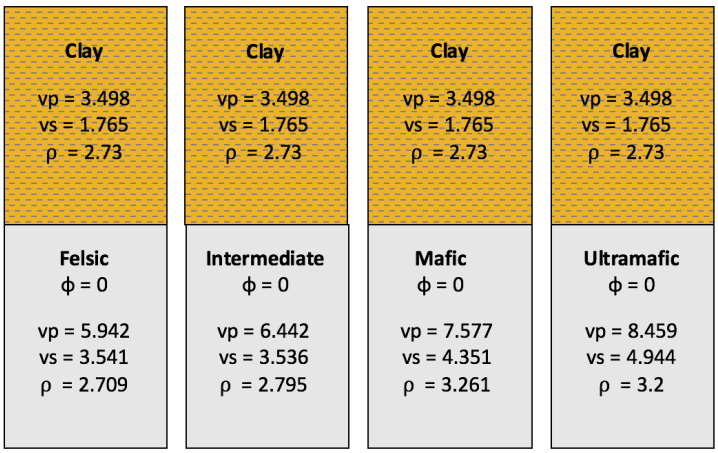

(b) $\phi = 0.05$

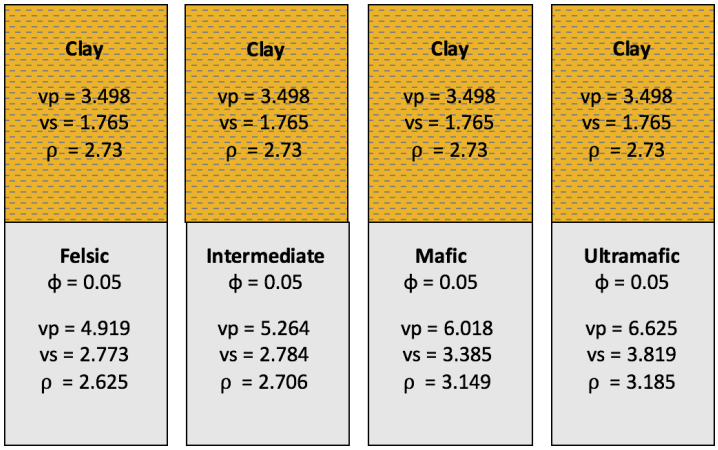

(c) $\phi = 0.1$

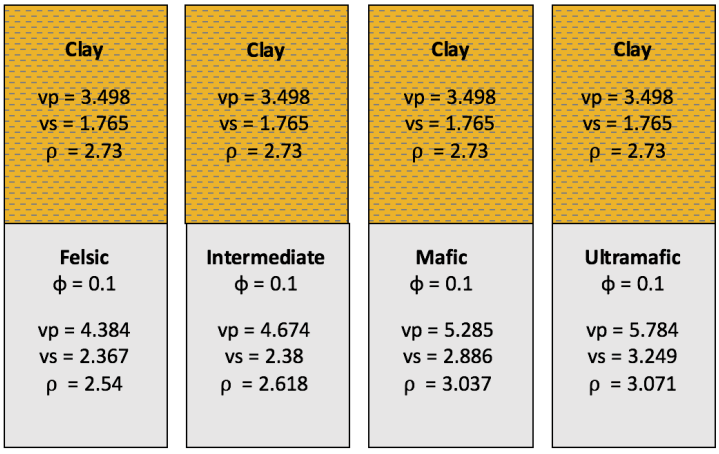

Figures 4.14 and 4.15 shows the 24 scenarios of half-space models for the cases of an overlying sedimentary half-space of sand and clay respectively. Zero porosity is considered for the overlying half-space, while the porosity of the basement changes from $\phi = 0$, $\phi = 0.05$ and $\phi = 0.1$. Section 3.6 describes the approach of obtaining the models.

4.8 P-P and P-S reflectivity

4.8.1 Reflectivity analysis

Reflectivity models are calculated for the interfaces shown in figures 4.14 and 4.15. Figures 4.16 and 4.17 shows the reflection coefficients for P-P reflection as a function of incident angle, calculated from the Zoeppritz equations. Correspondingly figures 4.18 and 4.19 shows the reflection coefficients for P-S reflection. The results for S-S reflectivity are shown in figures A.3 and A.4 in appendix. Figures 4.16 (P-P) and 4.18 (P-S) shows the cases for sand on top of basement, while figures 4.17 (P-P) and 4.19 (P-S) shows the cases for clay overlying the basement. Reflection coefficients are shown for the case of zero porosity, 5% porosity and 10% porosity for the categorizations felsic, intermediate, mafic and ultramafic.

The general trend for P-P reflection is that the reflection coefficient generally increases with decreasing silica content (from felsic to ultramafic) and with decreasing porosity. Zero porosity yields the largest reflection coefficient and 10% porosity the smallest for each of the scenarios. For P-S reflection the reflection coefficient shows the opposite trend; an increase in silica content (from felsic to ultramafic) as well as a decrease in porosity yields a smaller reflection coefficient. Here, zero porosity yields the smallest reflection coefficient and 10% porosity the largest. The common trend for both P-P and P-S reflection is that low porosity, as well as low silica content yields the smallest critical angle.

For the case of P-P reflection, it is observed that the case of sand on top of basement (figure 4.16) yields smaller reflection coefficient for small incident angles than for the case of clay on top of basement (figure 4.17). The reflectivity for the case of sand as the upper layer is generally weak, especially for high silica content (felsic and intermediate), and the reflection coefficient is actually shown to be zero or slightly negative for some cases. Only some of the scenarios shows critical angle. The case of clay as the upper layer yields larger

Figure 4.16: P-P wave reflection coefficient as a function of incident angle for two layered model for the case of sand on top of basement. The variations in basement porosities are shown as solid line: $\phi = 0$, dashed line: ϕ=0.05, dotted line: ϕ=0.1.

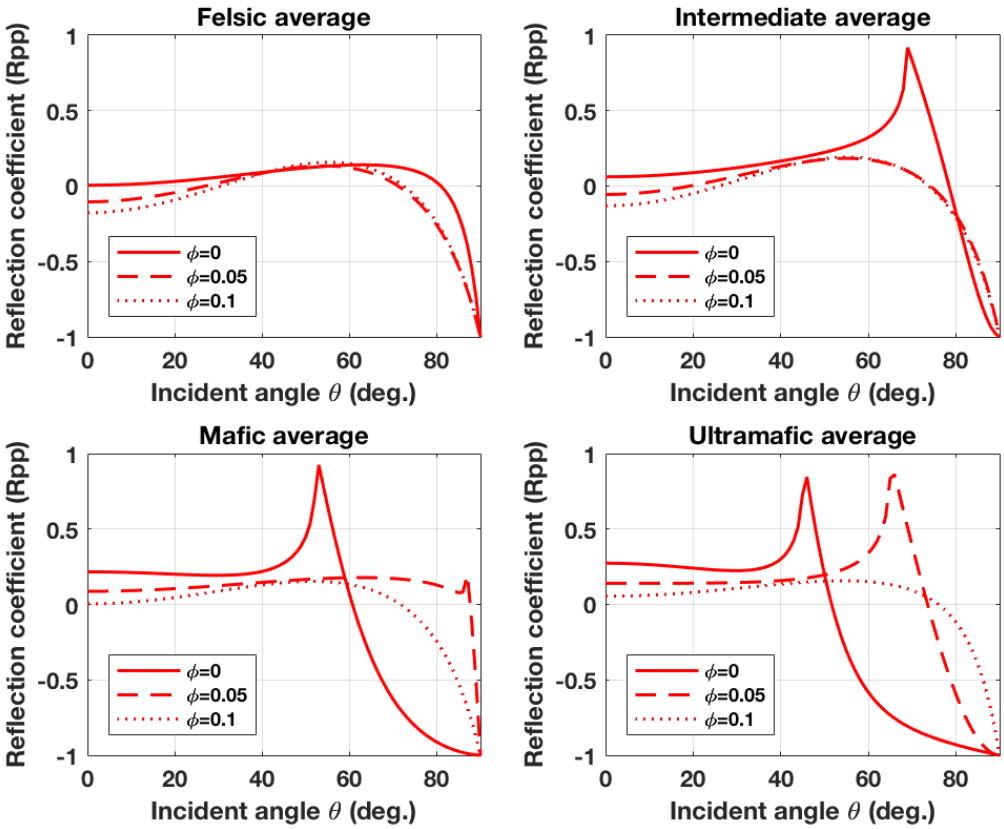

reflection coefficients than for sand, as well as smaller critical angles. In contrast to the case of sand as the upper layer, the reflection coefficients are all positive for cases, for incident angles smaller than the critical angle.

The case of P-S reflection also shows very small reflection coefficients for the case of sand on top of basement (figure 4.18). The reflection coefficients tends to be slightly positive for high silica content and slightly negative for low silica content. For the case of a clay on top of basement (figure 4.19) the reflection coefficients are stronger, but all negative. The critical angles are also generally quite small.

Figure 4.17: P-P wave reflection coefficient as a function of incident angle for two layered model for the case of clay on top of basement. The variations in basement porosities are shown as solid line: $\phi = 0$, dashed line: ϕ=0.05, dotted line: ϕ=0.1.

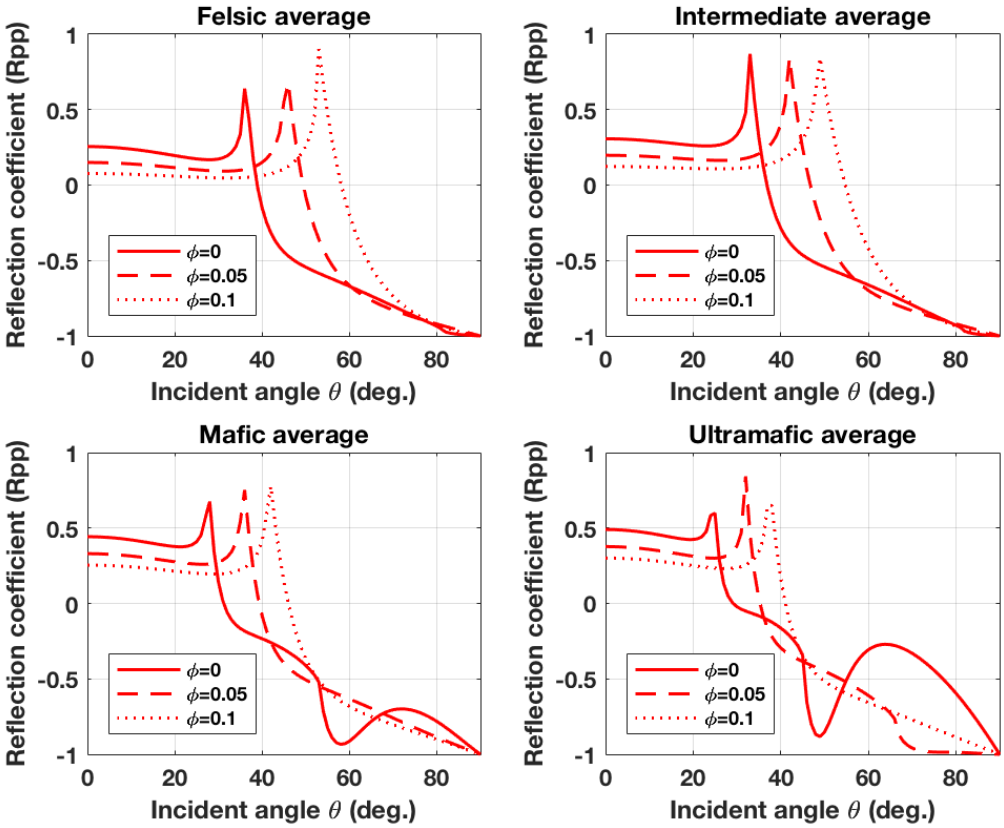

Figure 4.18: P-S wave reflection coefficient as a function of incident angle for two layered model for the case of sand on top of basement. The variations in basement porosities are shown as solid line: $\phi = 0$, dashed line: ϕ=0.05, dotted line: ϕ=0.1.

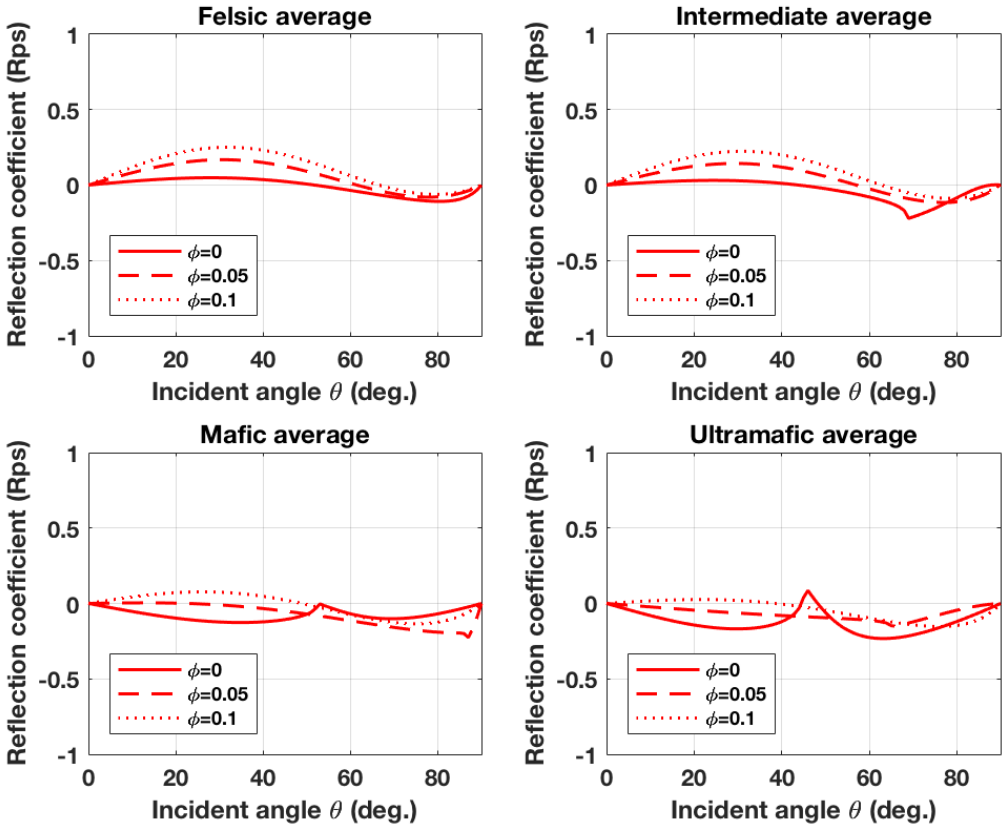

Figure 4.19: P-S wave reflection coefficient as a function of incident angle for two layered model for the case of clay on top of basement. The variations in basement porosities are shown as solid line: $\phi = 0$, dashed line: ϕ=0.05, dotted line: ϕ=0.1.

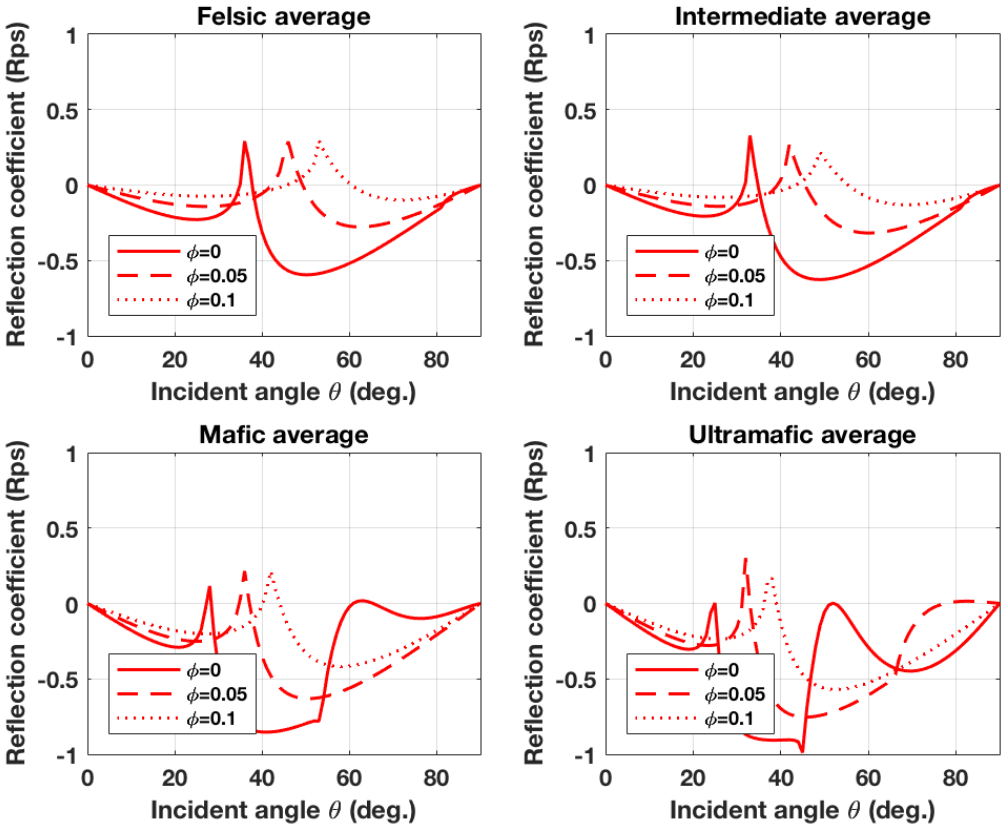

4.8.2 AVA-attributes

Figure 4.20 shows the intercept (R_0) versus gradient (G) for the half-space models (as seen in figures 4.14 and 4.15) for the case of P-P reflection. Figure 4.20a shows the scenario of sand as the upper layer, while 4.20b shows clay as the upper layer. The plot show the scenarios of zero porosity, 5% porosity and 10 porosity of the basement. The points represents felsic (yellow), intermediate (green), mafic (red) and ultramafic (blue).

For the case of clay as the upper layer (figure 4.20b), both felsic, intermediate, mafic and ultramafic plots in the fourth quadrant for all porosity cases, with positive intercept and negative gradient. For the case of sand as the upper layer (figure 4.20a) the points are distributed in the first and fourth quadrant for zero porosity, moving upwards towards the second quadrant with increasing porosity. The general trend for both plots is that the points move in a straight line north-west direction with increasing porosity or increasing silica content. The points for intermediate, mafic and ultramafic also forms a straight line, while the point for felsic plots outside this straight line, but still close to intermediate. Felsic and intermediate plots very close, and mafic and ultramafic also plots relatively close to each other. There is a larger separation between intermediate and mafic, and it is easy to see the separation low-silica versus high-silica content.

Figure 4.21 shows the intercept (R_0) versus curvature (C) for the half-space models, also for the case of P-P reflection. For the case of clay as the upper layer (figure 4.21a), all the points plots in the first quadrant with positive values for both intercept and curvature, moving towards southwest towards the axis origin. Figure 4.21a shows the case of sand as the upper layer. For zero porosity, the points plots in the first quadrant, except for felsic which plots in the axis origin. With increasing porosity, the points move towards southwest into the third quadrant slightly through the fourth quadrant. For all cases, the points forms approximately a straight line. The trend is that the points move towards the same southwest direction with increasing porosity or silica content. The separation between high-silica (felsic and intermediate) and low-silica (mafic and ultramafic) is still clear.

For the cases of felsic with zero porosity and mafic with 10%, it is shown that the intercept is equal to zero.

Figure 4.20: Gradient-intercept plot for the reflection of the interface between two layers. The lower layer varies in composition from felsic average, intermediate average, mafic average and ultramafic average, with basement porosities of 0%, 5% and 10%. a) shows the estimation of sand above basement, while b) shows the estimation of clay above basement.

(a) Sand above basement (b) Clay above basement

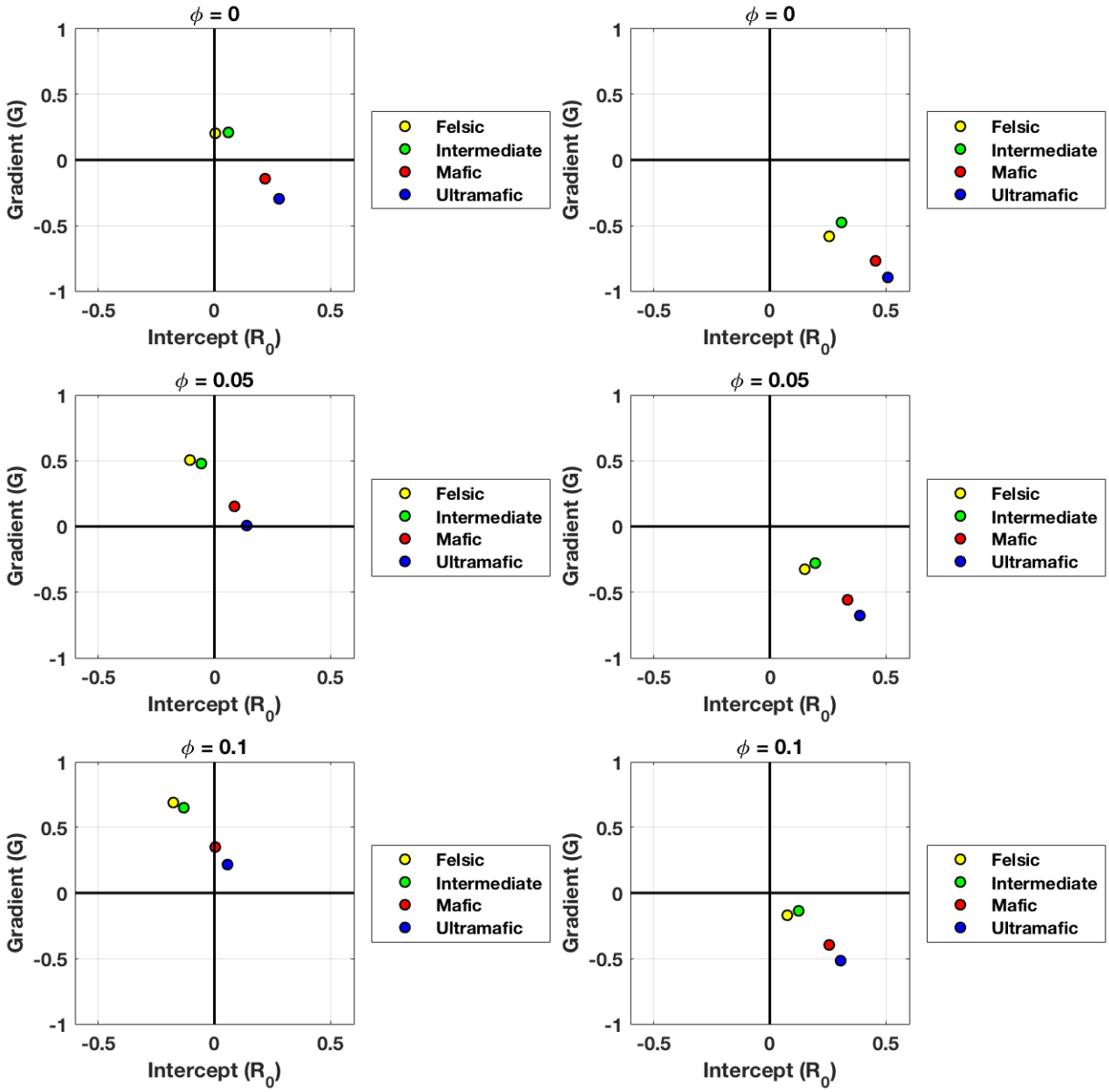

Figure 4.21: Gradient-curvature plot for the reflection of the interface between two layers. The lower layer varies in composition from felsic average, intermediate average, mafic average and ultramafic average, with basement porosities of 0%, 5% and 10%. a) shows the estimation of sand above basement, while b) shows the estimation of clay above basement.

(a) Sand above basement (b) Clay above basement

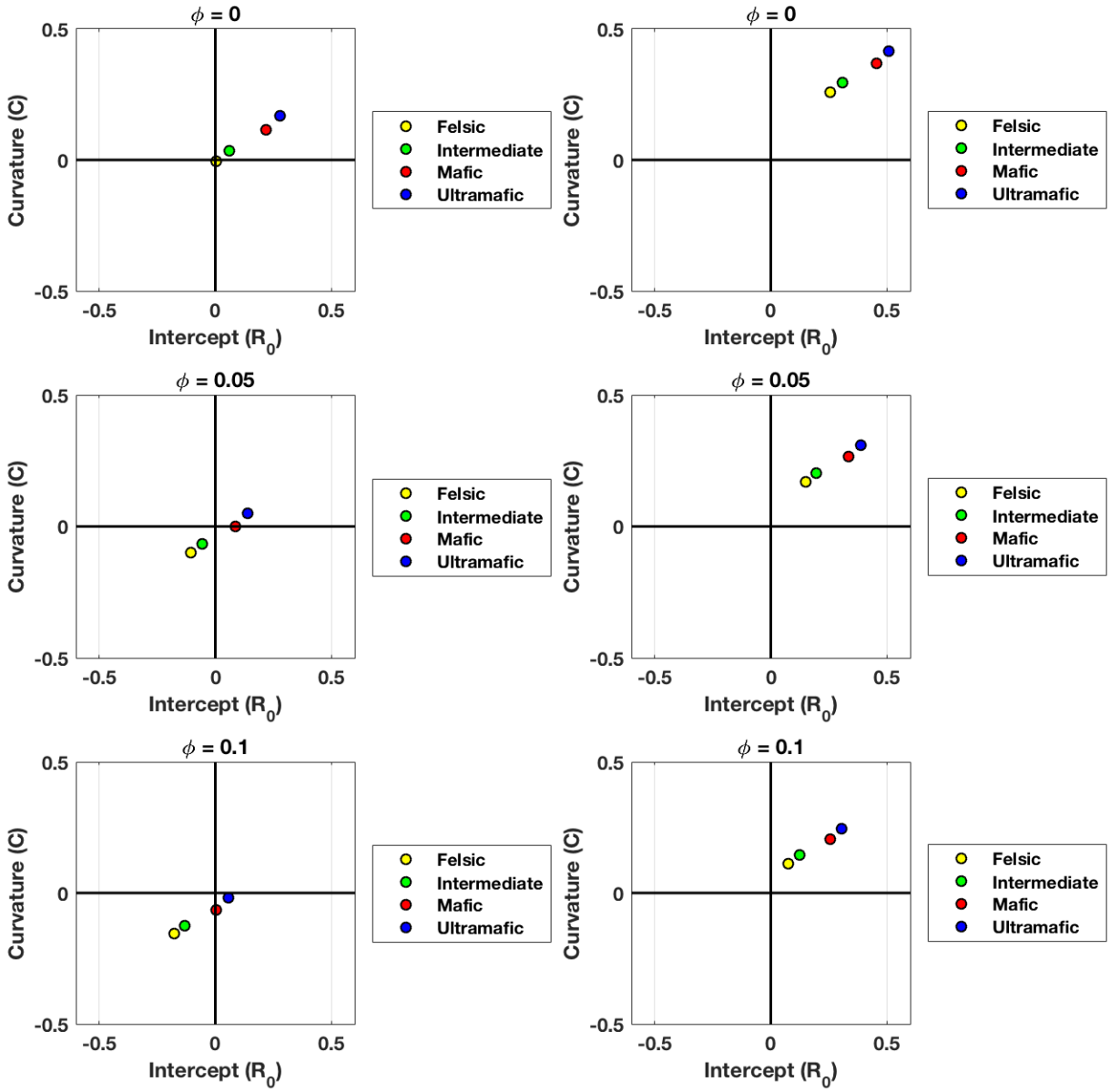

4.9 Basement reflectivity and the COB

The location of the seismic line in the Norwegian Sea offshore Norway is shown in figure 4.22, and figure 4.23 shows the seismic section from NW (left) to SE (right). The vertical axis represents the two-way traveltime (TWT) in milliseconds and the horizontal axis the line trace. Figure 4.24 shows the interpretation of the seabed and the basement. It can be observed from the map that SE should be the direction of the continental shelf. The fact that the section is slightly tilted upwards in the SE direction, and the depth to the seafloor is larger in the NW direction than in the SE direction also indicates that the transition from oceanic crust to continental crust is in the SE direction. We know that the continental crust is generally much thicker than the oceanic crust (Barton (2006) and Christensen and Mooney (1995)).

The basement was hard to interpret in the most NW part of the section, because the strength of the reflector was very weak and hard to identify, but basement was interpreted around 4500-6000 ms. Moving further in the SE direction the basement reflector generally has a good amplitude, and the basement tends to be strongly raised around line traces 6320 and 7314 up to almost 2000 ms. In the SE part of the section, the basement reflector was also generally very weak, and it was hard to pick the basement reflector because of very low amplitude. This part of the section shows a huge graben-feature with sedimentary innfill, which is typical for continental crust (D.V. Reddy, 2013), and the basement reflector tends to move deeper to around 6000 ms. Further towards SE the basement is again uplifted to around 2000 ms, and the amplitude of the reflector is again strong. Figure 4.25 shows the section fully interpreted with sedimentary packages and faults.

From the observation of the seismic section, the COB was interpreted to be around shot point 6320. It was hard to set an exact boundary because it is most likely that the section represents an area with transitional crust, and not a clear limit. The strong incline from NW until line trace 6320 most probably corresponds to a thickening of the crust in the transition from oceanic to continental crust. The horst-graben feature reinforces the fact that this should represent continental crust. The reason for the excact COB pick is the fact that the basement reflector weakens at the start of the graben. But the fact that the basement

Figure 4.22: Overview of the location of the seismic line and the wells available

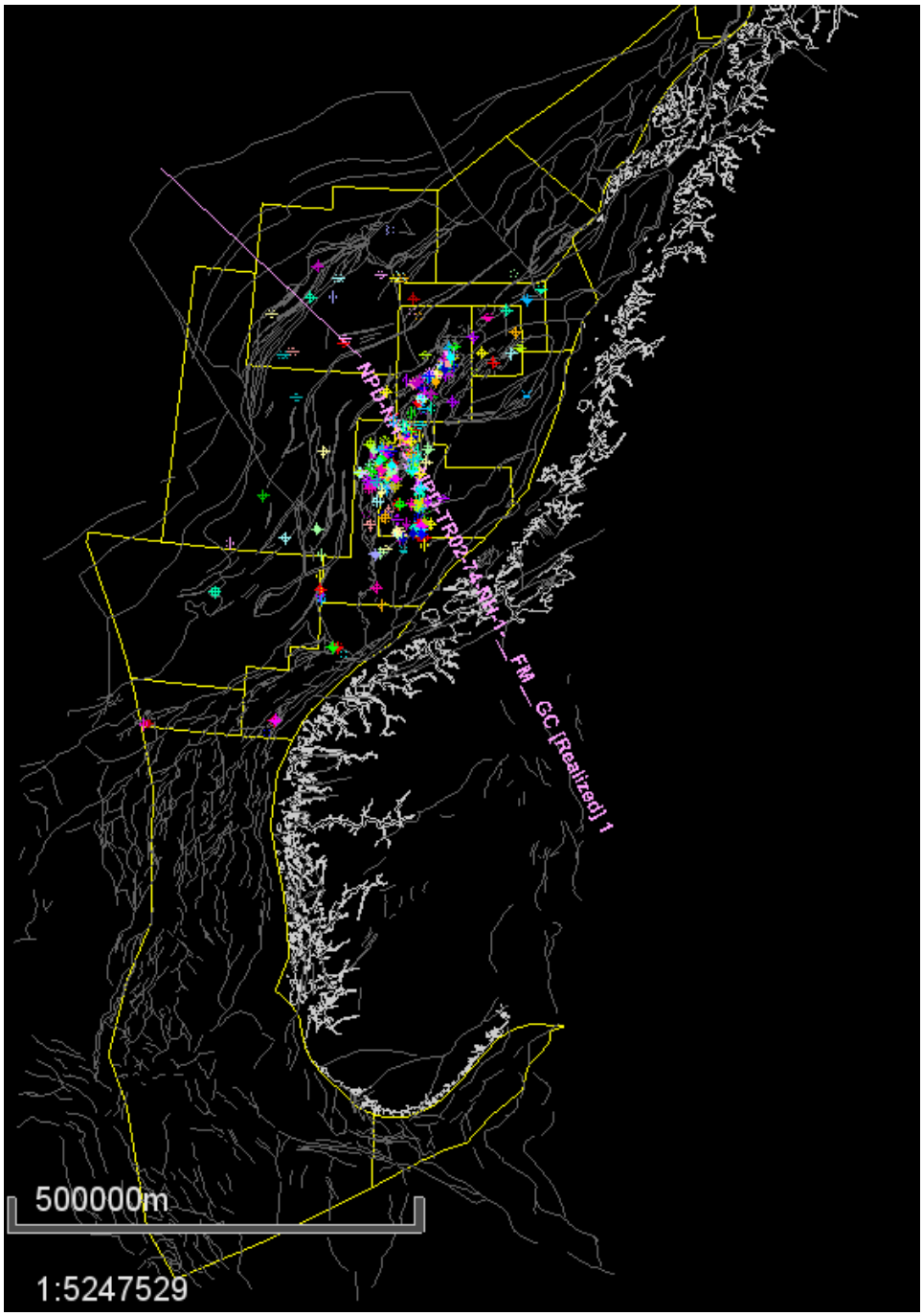

reflector is also very weak at the most NW part of the section which should represent oceanic crust, and that the basement reflector is strong at the most SE part which should represent continental crust, makes it hard to trust the strength of the reflector alone. For this section, the strength of the reflector also seems to be correlated with the depth of the reflector. Generally the amplitude seems to be higher where the basement is shallow, and the reflector is hard to interpret where the basement reflector is deep. This might be explained by poor processing or an increase in the porosity of the overlying sedimentary layer. At shallower depths it is more likely that the porosity is higher, resulting in a larger contrast at the interface.

Figure 4.23: Seismic section NPD-NH-79_NPD-TR02-74-NH-1-_FM_GC with COB pick

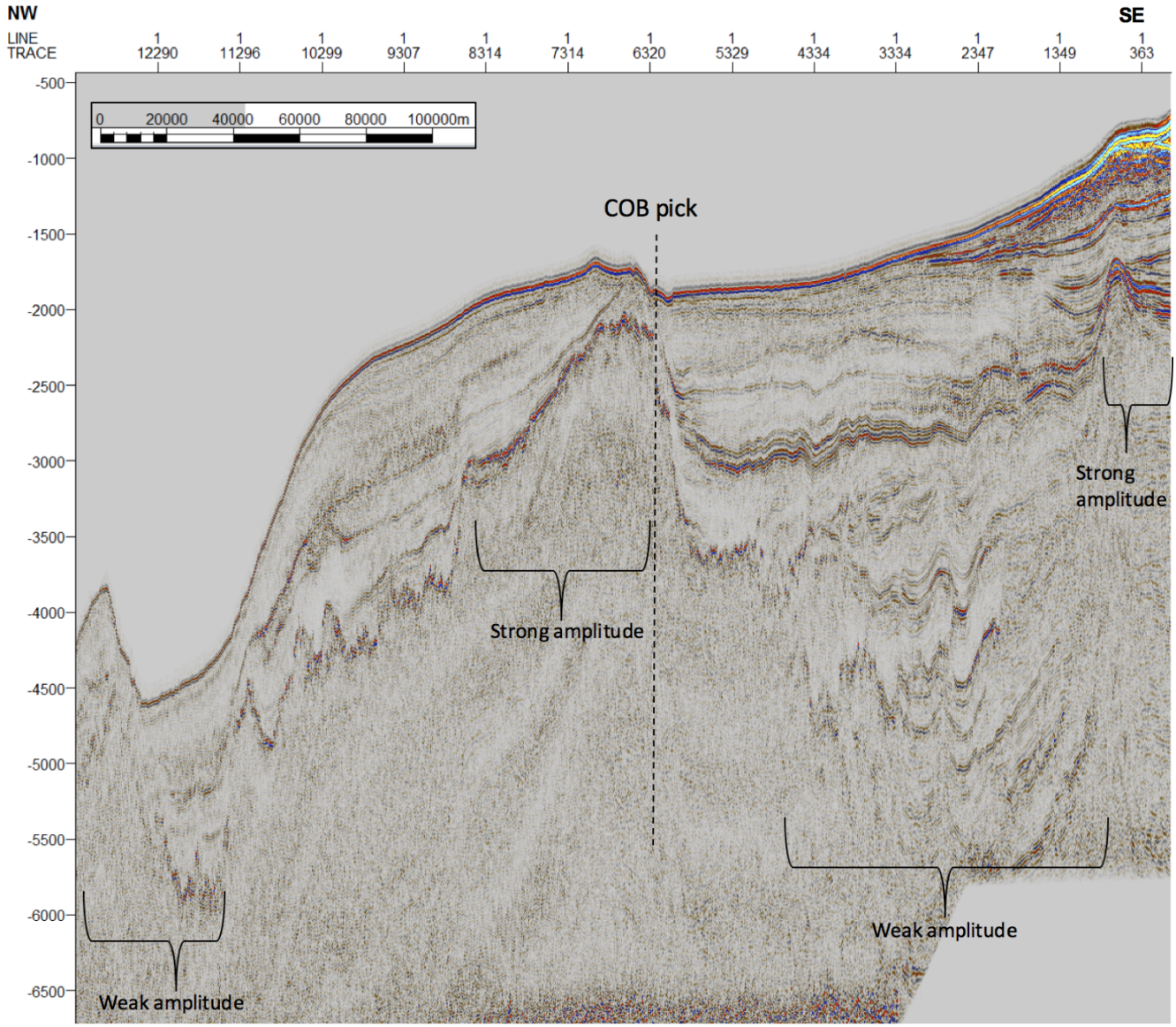

Figure 4.24: Seismic section NPD-NH-79_NPD-TR02-74-NH-1-_FM_GC interpretation of seabed and basement

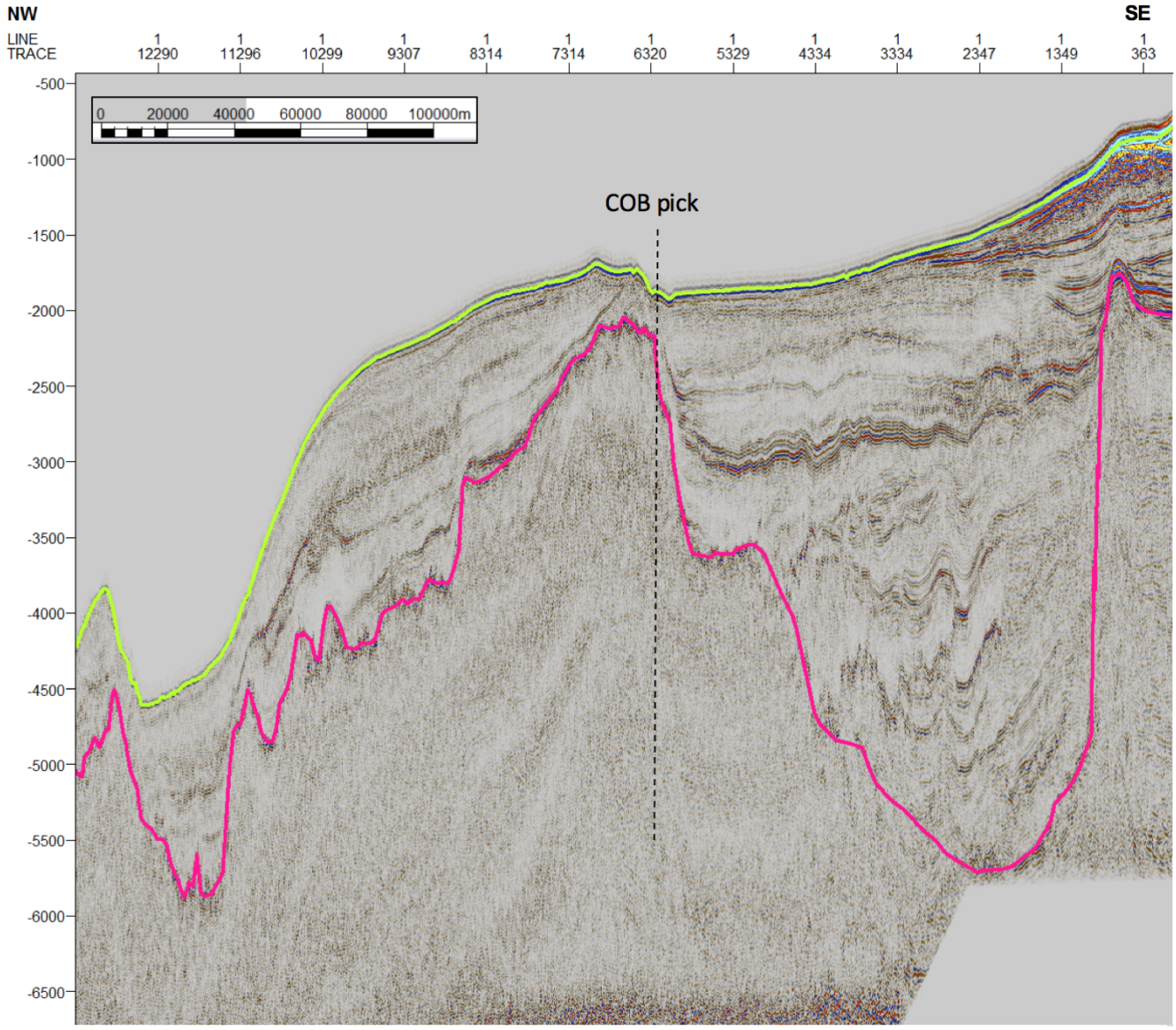

Figure 4.25: Seismic section NPD-NH-79_NPD-TR02-74-NH-1-_FM_GC interpretation of seabed, basement, sedimentary packages and faults

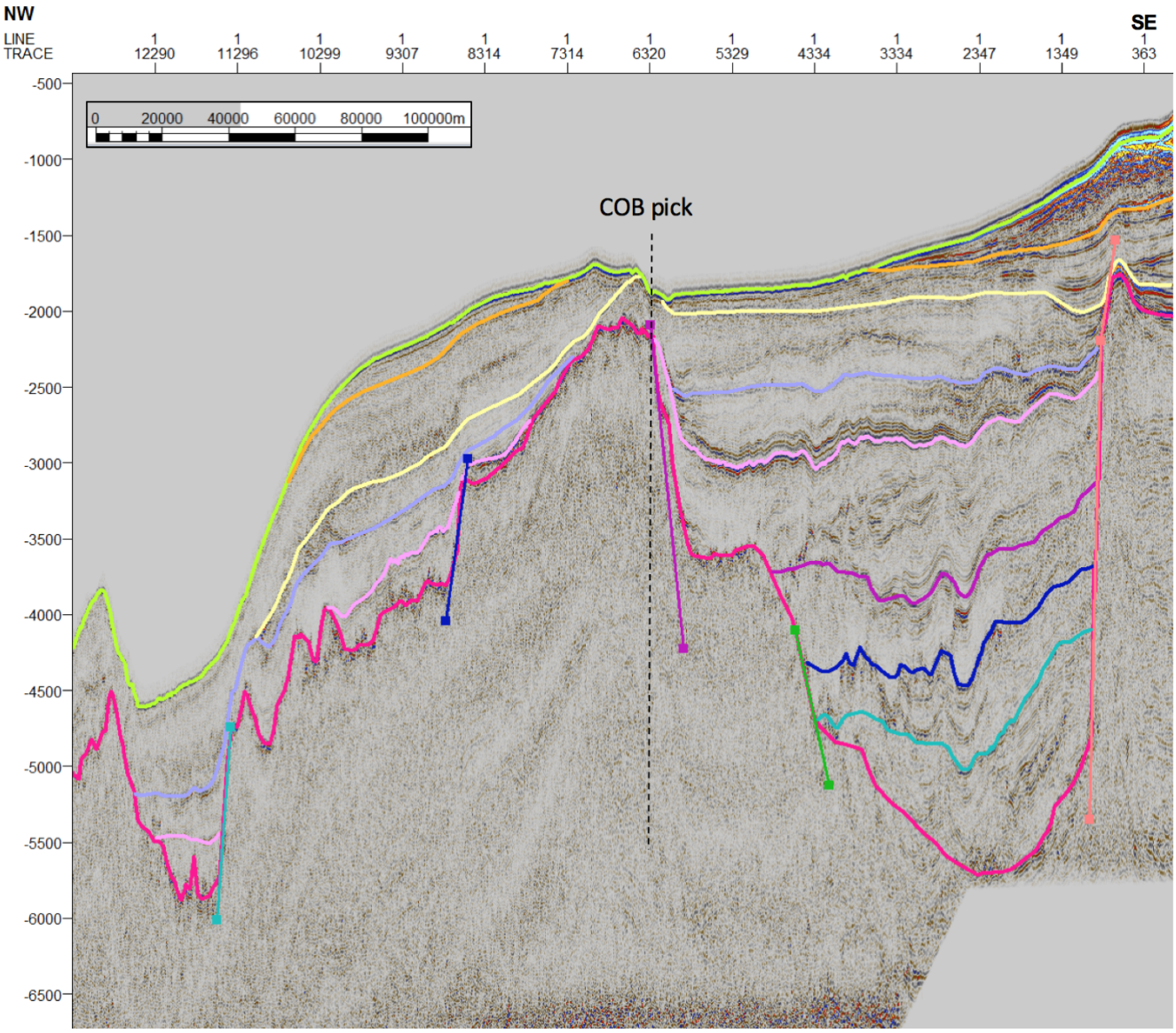

Chapter 5

Discussion

5.1 Reliability of the classification model and the mineral data

As earlier mentioned, average mineral values were used for each mineral phase. In reality these values varies due to individual variations in the properties of the mineral phases. There are usually several subgroups of minerals within each mineral group. This implies that there may be chemical differences, differences in crystal systems and sometimes polymorphs within each mineral groups that changes from one case to another. For example for plagioclase, there are Na-rich (Albite) and Ca-rich (Anorthite) plagioclase that will differ in the value of bulk modulus, shear modulus and density. Another example is pyroxene, where there are several subgroups of both clinopyroxene and orthopyroxene, examples from our data includes jadeite, bronzite and enstatite. The average values used in the calculations are based on all available data for each mineral group, and may not be a representative average of the natural occurrence in igneous rocks.

Igneous rocks usually also contain other, less abundant minerals than the minerals phases presented in the classification model (figure 3.1). The classification model is not entitled to these specific minerals phases to be present in order to fall under one of the classifications. The variation of minerals in igneous rocks is large and complex. The model does function as a guideline of what minerals is usually seen in igneous rocks for a certain presence of silica,

and minerals that are not abundant are therefore excluded from this simplified and general model. This implies that the velocity bounds obtained may not be accurate for all igneous rocks. Even though they fall under a certain category based on their silica content, the mineral composition may be significantly different. But the bounds still show the important trends that we were looking to show.

5.2 Accuracy of the Hashin-Shtrikman bounds

The Hashin-Shtrikman bounds obtained in this thesis are calculated from the mineral values based on the classification model, as discussed in the above section. This implies that the uncertainties associated with the mineral properties and the model also applies to the Hashin-Shtrikman bounds. The bounds in itself are proven to be accurate for a certain composite given that the fractions of the constituents are known, and their properties and mineral fractions are accurate. Therefore, bounds to account for all real occuring igneous rocks with their individual variations in composition are hard to obtain. But as we can see from the data plots (figures 4.3, 4.4, 4.5 and 4.6) the data for each classification groups generally plots well in between the bounds.

Even though the bounds are broader for low silica content than for high silica content, the velocity data generally shows a larger spreading for felsic rocks (high silica content) than for ultramafic rocks (low silica content). Some of the data for felsic rocks even plots just outside the bounds. This may be caused by the wrong estimate of porosity, but still the spreading in velocities is large. This observation may indicate that there is a larger spreading in velocities for rocks with high silica content than for low silica content, opposite of the trend shown by the the calculated bounds, and may further suggest that the bounds for felsic rocks should be somewhat broader for low porosities.

The bounds are generally quite broad, because they are to count for the possible geometric details of how the phases are arranged relative to each other, which is the unknown factor for predicting the effective elastic moduli for a mixture of grains and pores with given properties and fractions. Therefore an estimated average, here the Hashin-Shtrikman average, is useful in order to give an estimate of the elastic moduli for a certain content of silica. From the

observation of the data plots, this average seems to be a good estimate for the P-wave velocity. However, it is clear the Hashin-Shtrikman average for the S-wave velocity is way too low, as the data points generally plots closer to the upper bounds than the average.

The too low value of the estimated average for the S-wave velocity can be explained by the lower Hashin-Shtrikman bound for the shear modulus, which is zero for all porosities except for zero. As a consequence, the lower bound for the S-wave velocity is then also zero for all porosities except for zero, as the S-wave velocity depends directly of the shear modulus. This is a clear disadvantage of the Hashin-Shtrikman bounds for the case of including a pore fluid, as the shear modulus, and hence the S-wave velocity never actually gets close to zero for real occurring rocks. Because of this, the Hashin-Shtrikman average estimate for the S-wave velocity cannot be used as a realistic approach.

In order to perform a correction for this effect, bound fluid could be assumed for low porosities. The shear modulus for bound fluid is larger than zero, and therefore the lower S-wave velocity bound would be different from zero for low porosities. This would produce a better result, and a more accurate lower bound for low porosities, as the bounds for low porosities are of most interest.

5.3 Velocity plots and modification of measured velocity data

The data for basalt (Matthews, 1978) contained velocities from core measurements for standard pressure and temperature conditions, as well as porosities, so this data did not need to be modified in order to be plotted into the bounds. However, the data from Birch (1960) and Simmons (1964) could not be plotted directly into the bounds, because only densities were given, not porosities. Also, for the P-wave velocity data (Birch, 1960), the velocities were only given for pressures of 1 MPa ($\approx$ 10 atm) and higher.

As earlier mentioned, the estimation of porosity from the bulk density of the samples resulted in negative porosities for some samples. This implies that the estimation of porosity is generally poor. The solid density is only set to a estimated value based on the classification model, and does not represent the actual solid density of the sample. The estimated porosities

give an indication of the density of the sample compared to the estimated solid density for the average silica content for that classification, but the estimated porosities are not reliable. If the specific silica content of the rock samples was given, estimated solid densities could be calculated more specifically for that wt% silica, instead of a single mean density for a range within that categorization. This would cause the estimated porosities to be more accurate.

Generally, by extracting core samples from significant depths, there is a risk of formation of cracks caused by a rapid decrease in pressure. This change in stress conditions will cause the rock sample to expand quickly. The formation of cracks will cause the measured velocity to be lower than the actual velocity of the rock before compaction, and because these samples were measured at standard pressure and temperature conditions in the lab, this effect represents an uncertainty in the measured velocities of the rock samples extracted from significant depths. As earlier mentioned, the estimated P-wave velocities for standard pressure were estimated by a logarithmic approach, based on the velocity data for pressures ranging from 1 MPa to 1000 MPa. There is of course an uncertainty related to the use of this estimation as well, especially since the change in velocity is very steep for low pressures, even though the pressure interval between 1 and 0.1 MPa is very small compared to the total pressure interval. The velocities estimated for standard pressure conditions of 0.1 MPa is generally estimated to be significantly lower than the velocities for 1 MPa. The fact that velocity measurements for high stress conditions plots outside of the Hashin-Shtrikman bounds is an interesting observation, as the bounds should be designed to account for all textural variations of a given composite. However, the case of high stress conditions are not specified directly in the descriptions of the bounds, and mineralogical changes in the composition may also occur for high pressures. This observation may indicate that the Hashin-Shtrikman bounds are not designed to account for high stress conditions.

As the properties of the fluid were calculated with an assumption of a certain salinity of 35 000 ppm, there is an uncertainty related to the properties of the fluid that fills the pore space in the measured rock samples, as these properties were not specified. Due to the fact that igneous rocks generally have very low porosities, the effect of changes in fluid properties does not give a very large impact on the measured velocity data.

Even though there is a fair representation of different igneous rock samples, almost all the

samples are intrusive rocks, and a greater representation of extrusive rocks would be desirable in order to investigate trends between these textural differences. Especially velocity data for rhyolite, which is the extrusive equivalent to granite, would be desirable. Granite and basalt, which are the most abundant rocks in the continental and the oceanic crust respectively, are well represented (except for S-wave velocities for basalt), and they also plots well in between the bounds for their classification.

In order to achieve a more accurate estimation, the composition of the rock samples, and especially data regarding their silica content would be desirable. It is assumed that the silica content of the rock samples plots in between the upper and lower values determined by the classification model, based on their categorization. But these upper and lower limits may not be exactly accurate, and a three dimensional representation of the data points based on their silica content would better illustrate how they plot compared to the bounds due to silica content.

5.4 The effect of variations in texture

In order to model the variations in texture that causes the upper and lower Hashin-Shtrikman bounds for elastic properties, the self-consistent approximation was applied. The self-consistent approximation only accounts for differences in pore geometries, and not the sizes of the pores. Spherical pores represents stiff pores, while penny-shaped pores represents soft pores, and application of the self-consistent approximation shows that stiff pores generally results in higher elastic moduli than soft pores. Also, higher aspect ratio results in softer pores than for lower aspect ratios. For the estimation of the self-consistent approximation, the termination tolerance for the convergation was set as 1e-15, so there is reason to believe that the results are accurate.

Normal occurring pores will never be idealized geometrical shapes as perfect spheres or penny-shaped pores, and they are varying both in sizes and shapes. Those idealized geometrical shapes are only a simplification of various shapes than may occur. Surface or near surface rocks may contain pores that are nearly spherical in shape, but rocks exposed to high overburden pressure will normally contain pores that are more penny-shaped or flat

due to compaction. Normally, compaction will also cause the total porosity of the rock to decrease. Basement rocks generally has very low porosities compared to sedimentary rocks.

An other feature that should be modelled, is the effect of changes in grain size, in order to investigate the differences between extrusive and intrusive igneous rocks. While extrusive rocks normally crystallizes quickly due to rapid cooling when the magma reaches the surface, intrusive rocks crystallizes slowly before the magma reaches the surface. This results in small grain size for extrusive rocks, and larger grain size characterizing intrusive rocks. From figure 4.5, it is observed that gabbro and diabase samples generally measures higher velocities than basalt. This observation might indicate that grain size affects the elastic moduli, and that intrusive rocks generally has larger elastic moduli than volcanic rocks. But this observation alone is not enough to draw a conclusion. There might be other interfering factors that causes these differences in velocities. For example that the data is extracted from different sources. More velocity data from intrusive and extrusive equivalents would be desirable in order to investigate this further.

5.5 Trends of thermal and electrical properties

The observation from figure 4.11 is interesting, because the plots of thermal conductivity and electrical conductivity shows quite opposite trends. Figure 5.1 show the thermal and electrical conductivity for zero porosity as a function of silica content combined in one single plot, but with different axes units for thermal conductivity and electrical conductivity. This figure reinforces the earlier observation that there seems to be an opposite correlation between thermal and electrical conductivity. The fact that the mineral properties for thermal and electrical conductivity are extracted from different sources, emphasizes that the measurements are independent, and that this correlation is completely random.

This opposite correlation is most evident around 56 wt% silica, where the electrical conductivity shows its maximum value and thermal conductivity shows its minimum value. Their values are not to be compared, because they have completely different units and scales, but the trend that the electrical conductivity tends to be increasing where the thermal conductivity is decreasing, and opposite, is interesting. However, for high silica content (approximately

Figure 5.1: Thermal conductivity and electrical conductivity combined

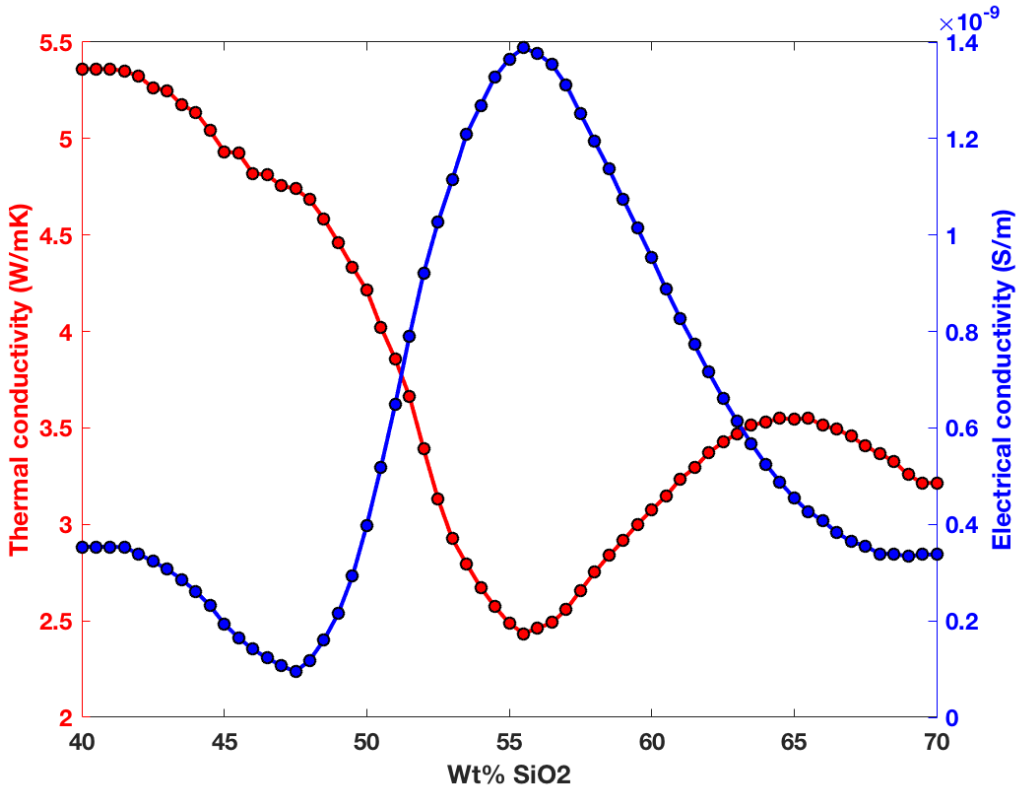

70-65 wt%) and low silica content (approximately 48-40 wt%) both the thermal and electrical conductivity show the same trend, they are both increasing with decreasing silica content. The opposite trend is shown through the whole intermediate classification, and parts of the mafic and felsic classifications (approximately 65-48 wt% silica). Ultramafic and parts of felsic and mafic classifications does not show the opposite trend.

The opposite correlation trend can be further explained by the electrical and thermal properties of the constituent mineral phases determined from the classification model as a function of silica. From the illustration of the classification model (figure 3.1), it can be observed that the mineral phases dominating the intermediate classification is plagioclase and amphibole. Micas (biotite and muscovite), quartz, orthoclase and pyroxene are also present. Table 3.3 shows the properties of each mineral phase. From the table it is shown that the micas, as well as plagioclase and orthoclase, show especially low thermal conductivities. Plagioclase also show the highest electrical conductivity of the mineral phases. Quartz stands

out as a special case, having both the highest thermal conductivity and lowest electrical conductivity of all the mineral phases. Because of its low electrical conductivity, quartz is considered to be an insulator.

5.5.1 The effect of fluid-filled pores

The distributions for thermal and electrical conductivity accounts only for solid rock with zero porosity. The effect of introducing porosity filled with a fluid would affect the conductivities to a large extent. Pure water has an electrical conductivity of $5.5{\cdot}10^{-6}$ S/m, which is much higher than for solid minerals. If the electrical conductivity was modelled as a function of porosity with water-filled pores, the electrical conductivity would increase drastically with increasing porosity. Brine has even higher electrical conductivity than pure water, because of its content of NaCl. For realistic cases with pores filled with brine, the electrical conductivity would be much higher than for the case of solid rock.

The reverse effect applies to thermal conductivity. Water has a thermal conductivity of approximately 0.6 W/mK which is significantly lower than for pure rock. However, compared to air and oil, water has the highest conductivity of the pore fluids. Introducing water-filled pores to the estimation of thermal conductivity, the thermal conductivity shows a decreasing trend with increasing porosity, the same way as shown for the elastic modulis. This trend can be observed from the model showing the Voigt and Reuss bounds for thermal conductivity in figure 4.12.

5.6 Accuracy of the half-space models

The half-space models are designed to simulate realistic interfaces between a sedimentary layer overlying an igneous basement. Because the basement is usually buried deep under several kilometers of sedimentary packages, the porosity can be assumed to be low. From the observation of the AVO, intercept-gradient and intercept-curvature plots, it is clear that there are great differences for the different cases of sand above basement and clay above basement. The properties for sand and clay were considered for the case of zero porosity. While the P-wave velocity for sand is above 6 km/s, the P-wave velocity for clay is approximately 3.5

km/s, which is a little more than the half of the sand velocity. The S-wave velocity for clay is below half of the S-wave velocity for sand. Their densities are not very different, but the estimated density for clay is a little higher than for sand. Sand and clay are both very common sedimentary rocks, but their elastic properties differ greatly. They are both likely to represent the sedimentary layer overlying the basement, but the reflectivity will vary greatly for these two cases. This is why the comparison between sand and clay is the most interesting when considering two different cases a sedimentary half-space overlying the basement.

The estimations for the basement considers the case of zero porosity, 5% porosity and 10 % porosity. The cases of felsic, intermediate, mafic and ultramafic represents average velocities and densities for that silica range considering the self-consistent approximation for a combination of spheres and penny shaped cracks with an aspect ratio of 0.01. Igneous basement rocks with porosities higher than 10% are rare, so the estimation of porosities up to 10% is a realistic approach.

In reality, the variations of interfaces with different velocities and densities are countless. Sedimentary rocks may have porosities up to 30% or higher near the surface, so the effect of porosity change in the upper sedimentary half-space should also be modelled to account for this effect. This would also consider the case of a shallow basement, where the porosities generally are higher for both the sedimentary and igneous rocks. However, this would result in a high number of combinations of velocity models to consider.

5.7 Basement reflectivity and determination of the COB

From the interpretation of the seismic section and the COB (section 4.9) it is shown that interpretation the COB based on the reflection amplitude alone may not be convincing, due to significant variations in reflection amplitude throughout the whole section. From the AVA-, intercept-gradient- and intercept-curvature plots produced from the theoretical models, several observations are made. The intercept-gradient and intercept-curvature plots shows that for the case of sand above basement, the reflection coefficient will either be weak positive, weak negative or equal to zero (for the cases of felsic with zero porosity, or mafic with 10% porosity). The case of clay as the overlying half-space will produce positive reflection

coefficient for all cases considered, however the reflection coefficient will be larger for low-silica rocks (mafic and ultramafic) than for high-silica rocks (felsic and intermediate). The reflection coefficient will also decrease with increasing porosity of the basement.

In short, the observation from the seismic section and the theoretical reflectivity (AVA) analysis both yields the same conclusion; The variations in properties of the sedimentary and igneous layers are too complex to set a general rule for the strength of the reflector. Especially it is seen that the cases of sand and clay as overburden half-spaces yields great variations in reflection coefficients, as well as critical angles. The AVA-, intercept-gradient and intercept-curvature plots are important for the explanation for why basement sometimes can be hard to interpret due to disappearance of the reflection amplitude. The strength of the basement reflector depends greatly on the velocity and density of the overlying sedimentary layer, and for the case of a high-velocity overburden such as sand the amplitude of the reflector may disappear completely. Where the basement is shallow, the porosities are likely to be higher than where the basement is deep, which will influence the strength of the reflector. The fact that the strength of the basement reflector tends to be weakening with increasing depth may also be explained by poor processing of the seismic, that the amplitudes may be more muted with increasing depth than for shallower depths.

However, the strength of the reflector can be a useful indicator, especially where the properties of the overlying sedimentary layer are known. Well data from wells that penetrates the overlying sedimentary layer will be very useful for the case of estimating the properties of the basement. Gravity and magnetic data will also be very useful in determination of the COB, as well as tectonic features like faulting, horst-graben structures and uplift.

The COB-pick around shot point 6320 is located further to the SE direction (and closer to the Norwegian coast) than the interpretation from Marcussen et al. (2009). By comparison of the localization of the seismic line (figure 4.22) with the interpretation shown in figure 3.2, Marcussen et al. (2009) shows a COB-pick corresponding to approximately line trace 11296 in the seismic section.

Chapter 6

Conclusions

From the results obtained by the application of the chemical classification model, the following main observations are done.

- The chemical classification model has shown to be a good approach in predicting the variations in geophysical properties of igneous rocks. From the Hashin-Shtrikman velocity bounds, it is seen that the core measurements representing natural occurrence of igneous rocks generally plots well inside the bounds for each of the classes; felsic, intermediate, mafic and ultramafic.

- The elastic properties generally show an increasing trend from high to low silica content and from high to low porosity. There is a strong correlation between density and elastic properties. The separation between low-silica composites (ultramafic and mafic) and high-silica composites (felsic and intermediate) is clear; the increase between intermediate and mafic is the most distinct, and the velocities seems to increase with a steeper rate for low-silica composites than high-silica composites.

- The geometry of the pores has shown to play an important role in controlling the elastic properties, the uncertainty represented by the upper and lower bounds. Spherical pores yields elastic moduli very close to the upper Hashin-Shtrikman bound representing very stiff pore shapes. Penny shaped cracks represents softer pores, and yields lower elastic moduli, depending on the aspect ratio of the cracks. The lower the aspect ratio, the lower the elastic moduli.

- Thermal and electrical conductivities shows quite different trends than for elastic properties. In fact, they show partly opposite trends. Thermal conductivity shows its minimum value where electrical conductivity shows its maximum value, around 56 wt% silica (intermediate classification).

- Reflectivity analysis shows that the reflection coefficient for P-P reflection generally will be larger for oceanic crust (low silica content) than for continental crust (high silica content) given the same overburden strata, but this observation alone is not sufficient for interpretation of the COB. The overburden sedimentary layer plays an important role in controlling the response, as well as other factors. Analysis of AVA-attributes shows cases where the intercept will be zero, which can explain why it sometimes can be hard to identify the basement reflector when interpreting seismic, especially on continental crust where the layer contrast is usually smaller than for oceanic crust. Increasing basement porosity also shows a decrease in P-P reflectivity.

Chapter 7

Further work

There are several areas that needs further investigation for a wider understanding of the geophysical properties of crustal igneous rocks. Some proposals for further work are listed below.

- The trends of intrusive versus extrusive igneous rocks should be further studied in order to investigate how their geophysical properties are affected by their differences in crystallization rate and grain sizes given their identical chemical composition. This would also help the investigation of continental crust versus oceanic crust, by focusing on the textural differences between basalt and granite.
- The COB offshore Norway should be further studied by using more seismic data, combined with well data from wells that penetrates the overburden, or most desirable the basement. Gravity magnetic data would also be useful for a more accurate determination of the COB.

Chapter 8

Acknowledgements

Firstly, I would like to express my great appreciation to my supervisor Kenneth Duffaut for his engagement and professional guidance. His willingness to give his time so generously has been very much appreciated.

I would also very much like to thank my co-supervisor Ketil Hokstad from Statoil for sharing his special expertise and research within this field, and for have taken the time to provide regular follow up.

I want to thank NTNU-NPD-SCHLUMBERGER PETREL READY database for providing me with seismic lines and well data for the use of identifying the COB.

Last but not least, I would like to thank my fellow students for their support and motivation throughout this semester.

References

Keiiti Aki and PG Richards. Quantative seismology: Theory and methods. *Freeman and Company*, 2, 1980.

K. S. Alexandrov and T. V. Ryzhova. Elastic properties of rock-forming minerals 2. layered silicates. *Bull. Acad. Sci. USSR, Geophys. Ser.*, 12, 1961a.

K. S. Alexandrov and T. V. Ryzhova. The elastic properties of crystals. *Sov. Phys. Crystallogr.*, 6, 1961b.

K. S. Alexandrov, T. V. Ryzhova, and B. P. Belikov. The elastic properties of pyroxenes. *Sov. Phys. Crystallog.*, 8, 1964.

K. S. Alexandrov, B. P. Belikov, and T. V. Rysova. Vycislenie uprugich parametrov gornich porod po mineralnomu sostavu. *Azv. Akad. Nauk. SSSR Ser. Geol*, 1966.

O. L. Anderson and R. C. Liebermann. Sound velocities in rocks and minerals. VESIAC State-of-the-Art Report No 7885-4-x, University of Michigan, 1966.

P. Avseth, T. Mukerji, G. Mavko, and J. Dvorkin. Rock-physics diagnostics of depositional texture, diagenetic alterations, and reservoir heterogeneity in high-porosity siliciclastic sediments and rocks - a review of selected models and suggested work flows. *Geophysics*, 75(5), 2010.

N. Barton. *Rock Quality, Seismic Velocity, Attenuation and Anisotropy.* CRC Press, 2006.

Michael Batzle and Zhijing Wang. Seismic properties of pore fluids. *Geophysics*, 57(11): 1396–1408, 1992.

J. G. Berryman. Mixture theories for rock properties. *Rock Physics and Phase Relations: a Handbook of Physical Constants*, pages 205–228, 1995.

F. Birch. The velocity of compressional waves in rocks to 10 kilobars, part 1. *Journal of Geophysical Research*, 65(4), 1960.

F. Birch. The velocity of compressional waves in rocks to 10 kilobars, part 2. *Journal of Geophysical Research*, 66(7), 1961.

R. S. Carmichael. *Practical Handbook of Physical Properties of Rocks and Minerals*. Boca Raton, FL: CRC Press, 1989.

N. I. Christensen and W. D. Mooney. Seismic velocity structure and composition of the continental crust: A global view. *Geophysical Research*, 100:9761–9788, 1995.

N. I. Christensen, R. H. Wilkens, S. C. Blair, and R. L. Carlson. Seismic velocities, densities, and elastic constants of volcanic breccias and basalt from deep sea drilling project leg 59. *Initial Reports of the Deep Sea Drilling Project*, 1980.

G.V. Reddy Dr. B.S. Josyulu D.V. Reddy, B.S.R Krishna. Identifying continental-oceanic boundaries in the eastern margin of india by seismic and gravity- magnetic data. *10th Biennial International Conference Exposition*, 2013.

D. Ellis, J. Howard, and C. Flaum. Mineral logging parameters: Nuclear and acoustic. *Tech. Rev.*, 36, 1988.

H. Gebrande. Elastic wave velocities and constant of elasticity of rock and rock forming minerals. *Physical properties of rocks*, 1, 1982.

E. K. Graham Jr. and G. R. Barsch. Elastic constants of single-crystal forsterite as a function of temperature and pressure. *Journal of Geophysical Research*, 74, 1969.

Z. Hashin and S. Shtrikman. A variational approach to the theory of the elastic behaviour of multiphase materials. *Journal of the Mechanics and Physics of Solids*, 11(2):127–140, 1963.

I. Koga, M. Aruga, and Y. Yoshinaka. Theory of plane elastic waves in a piezoeletric crystalline medium and determination of elastic and piezo-electric constants of quartz. *Phys. Rev.*, 109, 1958.

M. Kumazawa and O. L. Anderson. Elastic moduli, pressure derivatives, and temperature derivative of single-crystal olivine and single-crystal forsterite. *Journal of Geophysical Research*, 74, 1969.

Oyvind Marcussen, Brit I Thyberg, Christer Peltonen, Jens Jahren, Knut Bjorlykke, and Jan Inge Faleide. Physical properties of cenozoic mudstones from the northern north sea: Impact of clay mineralogy on compaction trends. *AAPG Bulletin*, 93(1):127–150, 2009.

W. P. Mason. Quartz crystal applications. *Bell Syst. Tech. J.*, 22, 1943.

D. Matthews. Shipboard measurements of seismic velocity, density, and porosity in dsdp leg 46 basalts. *Initial Reports of the Deep Sea Drilling Project*, 46:379–382, 1978.

Gary Mavko, Tapan Mukerji, and Jack Dvorkin. *The Rock Physics Handbook*. Cambridge, second edition, 2009.

H. J. McSkimin, P. Jr. Andreatch, and R. N. Thurston. Elastic moduli of quartz vs. hydrostatic pressure at 25 and 195.8 degrees celcius. *J. Appl. Phys.*, 36, 1965.

O Olesen, J Ebbing, E Lundin, E Mauring, JR Skilbrei, TH Torsvik, EK Hansen, T Henningsen, P Midbøe, and M Sand. An improved tectonic model for the eocene opening of the norwegian–greenland sea: Use of modern magnetic data. *Marine and Petroleum Geology*, 24(1):53–66, 2007.

Gary R. Olhoeft. Electrical properties of granite with implications for the lower crust. *Journal of Geophysical Research*, 86(B2):931–936, 1981.

T. V. Ryzhova, K. S. Aleksandrov, and V. M. Korobkova. The elastic properties of rock-forming minerals, v. additional data on silicates. *Bull. Acad. Sci. USSR, Earth Phys.*, (2), 1966.

J. H. Schön. *Physical Properties of Rocks*, volume 65 of *Developments in Petroleum Science*. Elsevier, 2015a.

Jürgen H Schön. *Physical properties of rocks: Fundamentals and principles of petrophysics*, volume 65. Elsevier, 2015b.

G. Simmons. Velocity of shear waves in rocks to 10 kilobars, 1. *Journal of Geophysical Research*, 69(6), 1964.

G. Simmons. Single crystal elastic constants and calculated aggregate properties. *J. Grad. Res. Center, SMU*, 34, 1965.

Tai Te Wu. The effect of inclusion shape on the elastic moduli of a two-phase material. *International Journal of solids and structures*, 2(1):1–8, 1966.

Leon Thomsen. Weak elastic anisotropy. *Geophysics*, 51(10):1954–1966, 1986.

R. K. Verma. Elasticity of some high-density crystals. *Journal of Geophysical Research*, 65, 1960.

Lev Vernik and Mark Kachanov. Modeling elastic properties of siliciclastic rocks. *Geophysics*, 75(6):E171–E182, 2010.

A. F. Woeber, S. Katz, and T.J. Ahrens. Elasticity of selected rocks and minerals. *Geophysics*, 28, 1963.

Appendix A

Appendix

A.1 Batzle and Wang properties of brine

From Mavko et al. (2009) we find a method for calculating the properties of brine introduced by Batzle and Wang. The density of brine, ρ_{brine} (g/cm^3) is given by equation A.1.

$$\rho_{brine} = \rho_w + S\{0.668 + 0.44S + 10^{-6}[300P - 2400PS + T(80 + 3T - 3300S - 13P + 47PS)]\} \tag{A.1}$$

where ρ_w is the density of pure water given by equation A.2, S is the salinity in fractions of one (parts per million divided by 10^6), P is the pressure in MPa and T is the temperature in degrees Celcius ($^\circ C$).

$$\rho_w = 1+10^{-6}(-80T-3.3T^2+0.00175T^3+489P-2TP+0.016T^2P-1.3\cdot10^{-5}T^3P-0.333P^2-0.002TP^2) \tag{A.2}$$

Further, the acoustic velocity in brine, V_{brine} (m/s) is needed to calculate the bulk modulus of the brine (K_{brine}). The acoustic velocity is given by equation A.3.

ω_{00}= 1402.85	ω_{02}= 3.437·10^{-3}
ω_{10}= 4.871	ω_{12}= 1.739·10^{-4}
ω_{20}= -0.04783	ω_{22}= -2.135·10^{-6}
ω_{30}= 1.487·10^{-4}	ω_{32}= 1.455·10^{-8}
ω_{40}= -2.197·10^{-7}	ω_{42}= 5.230·10^{-11}
ω_{01}= 1.524	ω_{03}= -1.197·10^{-5}
ω_{11}= -0.0111	ω_{13}= -1.628·10^{-6}
ω_{20}= 2.747·10^{-4}	ω_{23}= 1.237·10^{-8}
ω_{31}= -6.503·10^{-7}	ω_{33}= 1.327·10^{-10}
ω_{41}= 7.987·10^{-10}	ω_{43}= -4.614·10^{-13}

Table A.1: Coefficients ω_{ij} for the method of Batzle and Wang

$$V_{brine} = V_w + S(1170 - 9.6T + 0.055T^2 - 8.5\cdot10^{-5}T^3 + 2.6P - 0.0029TP - 0.0476P^2) + S^{\frac{3}{2}}(780 - 10P + 0.16P^2) - 18 \tag{A.3}$$

where V_w is the acoustic velocity in pure water V_w given by equation A.4. The coefficients ω_{ij} are given by table A.1.

$$V_w = \sum_{i=0}^{4}\sum_{j=0}^{3}\omega_{ij}T^iP^j \tag{A.4}$$

The bulk modulus of brine (K_{brine}) is then given by equation A.5.

$$K_{brine} = \rho_b V_b^2 \tag{A.5}$$

A.2 Mineral properties

The mineral properties used for calculations of the elastic bounds (table 3.1) are arithmetic averages, based on the data available for each mineral phase. These arithmetic average values were simply computed from the properties shown in table A.2, showing a detailed view of the original sources for each set of properties. The data was originally obtained from (Schön, 2015a) Table 6.2 and (Mavko et al., 2009) table A.4.1, but these are only compilations of the original sources.

Mineral	**Subgroup**	**Bulk modulus** *(GPa)*	**Shear modulus** *(GPa)*	**Density** *(kg/m^3)*	**Original source**
Orthoclase	-	46.8	27.3	2570	1
Quartz	-	37	44	2650	2
	-	36.6	45	2650	3, 4, 5
	-	36.5	45.6	2650	6
	-	37.9	44.3	2650	7
	-	38.2	43.3	2650	8
Plagioclase	-	75.6	25.6	2630	9
	Anorthite	84	40	2760	8
	Albite	55	29.5	2630	8
Pyroxene	Diopside	111.2	63.7	3310	10, 11
	Augite	94.1	57	3260	11
Olivine	Forsterite	129.8	84.4	3320	12, 13, 14
	Forsterite	129.6	81	3224	8
	-	130	80	3320	2
Muscovite	-	61.5	41.1	2790	15
	-	42.9	22.2	2790	16
	-	52	30.9	2790	17
	-	52	32	2790	8
Biotite	-	59.7	42.3	3050	15
	-	41.1	12.4	3050	16
	-	51	27	3050	8
Amphibole	Hornblende	87	43	3124	8

Table A.2: Mineral properties. 1: Alexandrov et al. (1966), 2: Carmichael (1989), 3: Simmons (1965), 4: Mason (1943), 5: Koga et al. (1958), 6: Anderson and Liebermann (1966), 7: McSkimin et al. (1965), 8: Gebrande (1982), 9: Woeber et al. (1963), 10: Ryzhova et al. (1966), 11: Alexandrov et al. (1964), 12: Verma (1960), 13: Graham Jr. and Barsch (1969), 14: Kumazawa and Anderson (1969), 15: Alexandrov and Ryzhova (1961a), 16: Ellis et al. (1988), 17: Alexandrov and Ryzhova (1961b)

A.3 Hashin-Shtrikman 3D bounds

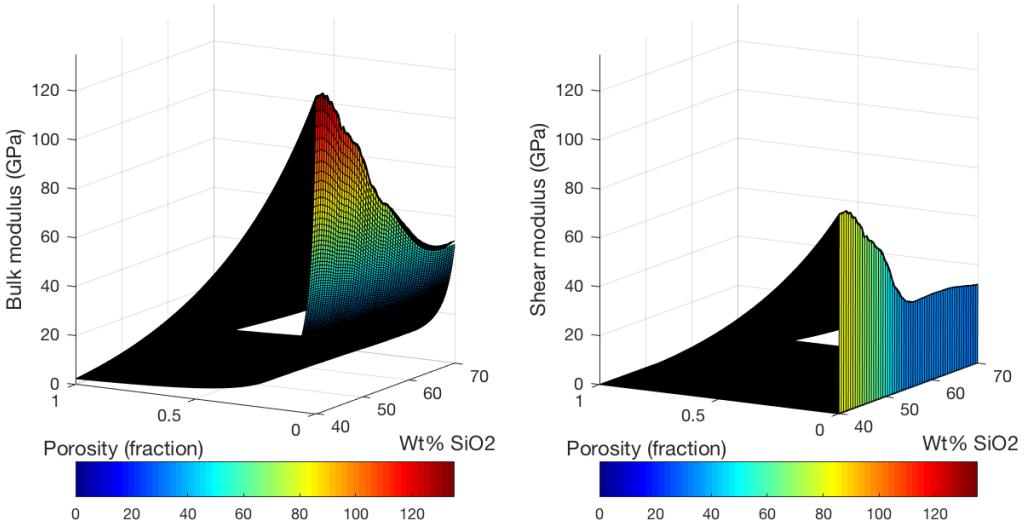

Figure A.1: 3D plot of the bulk and shear modulus upper and lower Hashin-Shtrikman bounds as a function of silica content and porosity

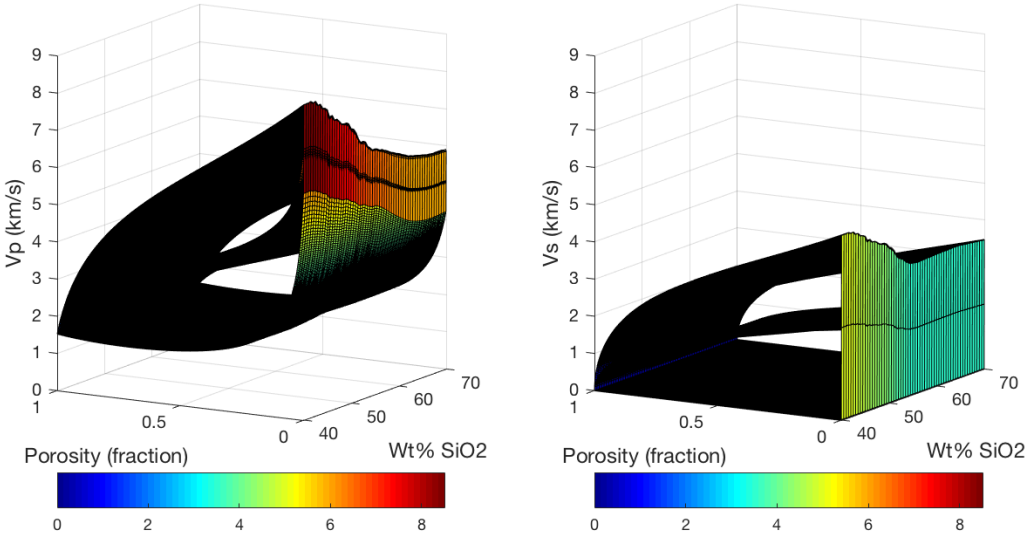

Figure A.2: 3D plot of the P- and S-wave velocity upper, lower and average (in between the upper and lower) Hashin-Shtrikman bounds as a function of silica content and porosity

A.4 Explicit solutions for the Zoeppritz equations

$$R_{PP} = \left[\left(b\frac{cos\theta_1}{V_{P1}} - c\frac{cos\theta_2}{V_{P2}}\right)F - \left(a + d\frac{cos\theta_1}{V_{P1}}\frac{cos_{S2}}{V_{S2}}\right)Hp^2\right]/D \tag{A.6}$$

$$R_{SP} = -2\frac{cos\theta_{S1}}{V_{S1}}\left(ab + cd\frac{cos\theta_2}{V_{P2}}\frac{cos\theta_{S2}}{V_{S2}}\right)pV_{S1}/(V_{P1}D) \tag{A.7}$$

$$R_{PS} = \left[-2\frac{cos\theta_1}{V_{P1}}\left(ab + cd\frac{cos\theta_2}{V_{P2}}\frac{cos\theta_{S2}}{V_{S2}}\right)pV_{P1}\right]/(V_{S1}D) \tag{A.8}$$

$$R_{SS} = \left[\left(b\frac{cos\theta_{S1}}{V_{S1}} - c\frac{cos\theta_{S2}}{V_{S2}}\right)E - \left(a + d\frac{cos\theta_2}{V_{P2}}\frac{cos\theta S1}{V_{S1}}\right)Gp^2\right]/D \tag{A.9}$$

The variables a, b, c, d, D, E, F, G and H are defined by equations A.10, A.11, A.12, A.13, A.14 A.15, A.16, A.17 and A.18 respectively.

$$a = \rho_2(1 - 2sin^2\theta_{S2}) - \rho_1(1 - 2sin^2\theta_{S1}) \tag{A.10}$$

$$b = \rho_2(1 - 2sin^2\theta_{S2}) + 2\rho_1 sin^2\theta_{S1} \tag{A.11}$$

$$c = \rho_1(1 - 2sin^2\theta_{S1}) + 2\rho_2 sin^2\theta_{S2} \tag{A.12}$$

$$d = 2(\rho_2 V_{S2}^2 - \rho_1 V_{S1}^2) \tag{A.13}$$

$$D = EF + GHp^2 \tag{A.14}$$

$$E = b\frac{cos\theta_1}{V_{P1}} + c\frac{cos\theta_2}{V_{P2}} \tag{A.15}$$

$$F = b\frac{cos\theta_{S1}}{V_{S1}} + c\frac{cos\theta_{S2}}{V_{S2}} \tag{A.16}$$

$$G = a - d\frac{cos\theta_1}{V_{P1}}\frac{cos\theta_{S2}}{V_{S2}} \tag{A.17}$$

$$H = a - d\frac{cos\theta_2}{V_{P2}}\frac{cos\theta_{S1}}{V_{S1}} \tag{A.18}$$

A.5 S-S reflectivity

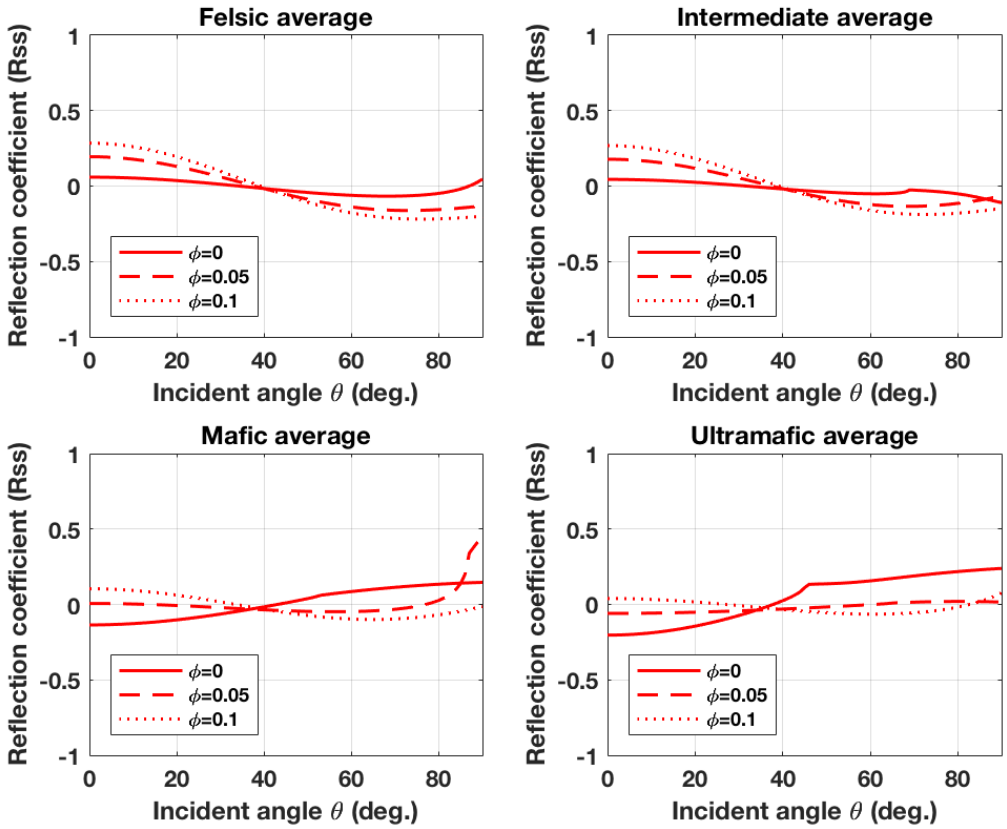

Figure A.3: S-S wave reflection coefficient as a function of incident angle for two layered model for the case of sand on top of basement. The variations in basement porosities are shown as solid line: $\phi = 0$, dashed line: ϕ=0.05, dotted line: ϕ=0.1.

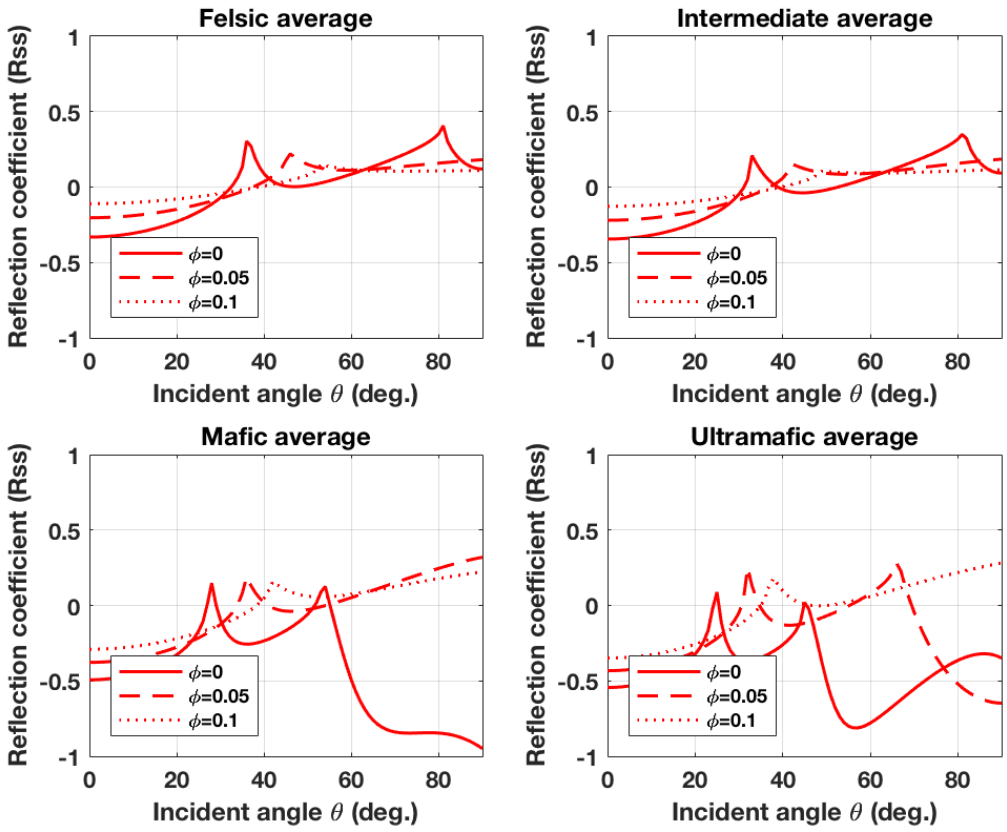

Figure A.4: S-S wave reflection coefficient as a function of incident angle for two layered model for the case of clay on top of basement. The variations in basement porosities are shown as solid line: $\phi = 0$, dashed line: ϕ=0.05, dotted line: ϕ=0.1.